Czech Technical University in Prague
Faculty of Nuclear Sciences and Physical Engineering
Department of Physics

Plasma environment of the Jupiter moon Io

Diploma thesis

Author: Bc. Ondřej Šebek
Supervisor: Ing. Pavel Trávníček, Ph.D.
Academic Year: 2009/2010

Zadání

Acknowledgements: I would like to thank Pavel Trávníček for his willing supervision and useful comments on the work. I thank also Petr Hellinger for helpful discussions on the plasma theory.

Prohlašuji, že jsem svou diplomovou práci vypracoval samostatně a použil jsem pouze podklady uvedené v přiloženém seznamu.

Nemám závažný důvod proti užití tohoto školního díla ve smyslu §60 Zákona č.121/2000 Sb., o právu autorském, o právech souvisejících s právem autorským a o změně některých zákonů (autorský zákon).

V Praze dne 10. 9. 2010 Ondřej Šebek

Abstract

Název práce: **Prostředí plazmatu v okolí Jupiterova měsíce Io**

Autor: Ondřej Šebek

Obor: Fyzikální inženýrství

Druh práce: Diplomová práce

Vedoucí práce: Ing. Pavel Trávníček, Ph.D., Astronomický ústav, AV ČR

Abstrakt: Práce se zabývá interakcí mezi měsícem Io a Jupiterovým magnetosférickým plazmatem. Interakce byla modelována dvourozměrným hybridním kódem s částicovými ionty a tekutinou elektronů. V simulacích byl studován vliv vlastností ionosféry a atmosféry měsíce Io na tvorbu nestabilit generovaných teplotní anizotropií plazmatu. Konkrétně byly měněny hodnoty iontové produkce způsobené elektronovou ionizací a fotoionizací a hustoty neutralní atmosféry, která určuje četnost nábojových výměn mezi ionty plazmatu a atmosférickými neutrály. Fluktuace magnetického pole a hustoty plazmatu jsou výrazné hlavně na návětrné straně Io při střední a vysoké hodnotě iontové produkce. Zvýšení četnosti nábojových výměn snižuje fluktuace. Na návětrné straně je pozorována antikorelace mezi oscilacemi magnetického pole a hustoty plazmatu, která může svědčit o růstu zrcadlové nestability.

Klíčová slova: Io, nestability plazmatu, hybridní simulace

Title: **Plasma environment of the Jupiter moon Io**

Abstract: This work deals with the interaction of volcanic moon Io with Jovian magnetospheric plasma. We study the interaction by means of hybrid two-dimensional simulations with kinetic ions and fluid electrons. We change properties of Io's ionosphere and neutral atmosphere to study their effects on the generation of temperature anisotropy driven instabilities. First we change the ion production rate due to the photoionization and electron impact ionization at Io and second we use variable density of Io's atmosphere to change the rate of charge exchanges between plasma ions and atmospheric neutrals. Fluctuations in magnetic field and plasma density are present mainly upstream of Io in simulations with moderate and high ion production rate. Increase of the charge exchange rate reduces the fluctuations. We observe anticorrelation between oscillations of magnetic field and plasma density upstream of Io. This anticorrelation may indicate the growth of mirror instability.

Key words: Io, plasma instabilities, hybrid simulations

Contents

Introduction

This work deals with the interaction of the Jupiter moon Io with Jovian magnetospheric plasma. Io is a volcanic moon which continually feeds the Jovian magnetospheric plasma with new particles. The plasma originating from Io forms a plasma torus which corotates with Jupiter and interacts strongly with Io, its atmosphere and ionosphere.

The fresh plasma from Io has large temperature anisotropy and may become unstable through the temperature anisotropy driven instabilities. Waves triggered by these instabilities have been observed at Io during several flybys of satellite *Galileo*.

The interaction is studied by means of hybrid two-dimensional numerical simulations with kinetic ions and fluid electrons. The attention is paid to the evolution of temperature anisotropy of plasma ions and generation of plasma waves driven by the temperature anisotropy in dependence on properties of Io's atmosphere. To be specific we change the rates of ionization processes at Io.

The work is organized as follows: in chapter 1 we introduce the temperature anisotropy driven instabilities which are relevant in the context of space plasma physics. Chapter 2 deals with the Io's plasma environment. In particular subsections we describe Io, its plasma torus and the interaction between them and we summarize observations of plasma waves at Io. In chapter 3 we present the simulation model used in this work and give an overview of previous studies of plasma torus interaction with Io by means of numerical simulations. In chapter 4 we discuss results of performed numerical simulations.

Chapter 1

Kinetic theory of plasma waves

Space plasmas are often magnetized and one of important parameters characterizing them is the temperature anisotropy between the directions parallel and perpendicular to the magnetic field. The space plasma can undergo several processes which increase or decrease the anisotropy. Once the plasma is not isotropic, the free energy associated with the anisotropy tends to drive an instability to isotropize the plasma. Observation of the anisotropy driven instabilities provides information about plasma composition and properties.

1.1 Dispersion relation in magnetized plasma

1.1.1 Kinetic approach

The basis of the kinetic approach is a distribution function $f(t, \mathbf{x}(t), \mathbf{v}(t))$ which describes the density distribution in the phase space $\mathbf{x} - \mathbf{v}$ at time t. Integration over the velocity space gives the number density at position $\mathbf{x}$

$$\int f(t, \mathbf{x}, \mathbf{v}) d^3\mathbf{v} = n(t, \mathbf{x}).$$

The total time change of the distribution function is given by the Boltzmann equation

$$\frac{df}{dt} = \frac{\partial f}{\partial t} + (\mathbf{v}\nabla) f + \left(\frac{1}{m}\mathbf{F}\nabla_v\right) f = C \tag{1.1}$$

where C is the collisional term which represents a time change of distribution function f due to collisions, m is particle mass and $\mathbf{F}$ is force acting on the plasma. Various forms of the Boltzmann equation differ in forms of the

collisional term and the force. The simplest approximation is the Vlasov equation

$$\frac{\partial f}{\partial t} + (\mathbf{v}\nabla)\, f + \left[\frac{q}{m}\left(\mathbf{E} + \mathbf{v}\times\mathbf{B}\right)\nabla_v\right] f = 0 \tag{1.2}$$

which holds for a collisionless plasma and the Lorentz force $\mathbf{F} = q(\mathbf{E}+\mathbf{v}\times\mathbf{B})$ acting on particles with charge q.

Vlasov equation can be used to solve some instabilities in the plasma. The problem is usually solved in a linear approximation. Quantities are expanded to the first order perturbation $\mathbf{B} = \mathbf{B}_0 + \delta\mathbf{B}$, $\mathbf{E} = \mathbf{E}_0 + \delta\mathbf{E}$ and $f = f_0 + \delta f$. If we assume zero background electric field and neglect terms with second order perturbation, the linearized Vlasov equation reads as

$$\frac{\partial \delta f}{\partial t} + (\mathbf{v}\nabla)\,\delta f + \left[\frac{q}{m}\left(\mathbf{v}\times\mathbf{B}_0\right)\nabla_v\right]\delta f = -\left[\frac{q}{m}\left(\delta\mathbf{E} + \mathbf{v}\times\delta\mathbf{B}\right)\nabla_v\right] f_0. \tag{1.3}$$

1.1.2 General dispersion relation

Let us derive a general dispersion relation of waves in magnetized plasma. We start with Ampér's and Faraday's laws:

$$\begin{aligned}\nabla\times\mathbf{B} &= \mu_0\epsilon_0\frac{\partial\mathbf{E}}{\partial t} + \mu_0\mathbf{j},\\ \nabla\times\mathbf{E} &= -\frac{\partial\mathbf{B}}{\partial t}.\end{aligned}$$

The magnetic induction $\mathbf{B}$ can be eliminated to get an equation for electric field $\mathbf{E}$

$$\nabla^2\mathbf{E} - \nabla\cdot(\nabla\mathbf{E}) - \mu_0\epsilon_0\frac{\partial^2\mathbf{E}}{\partial t^2} = \mu_0\frac{\partial\mathbf{j}}{\partial t}. \tag{1.4}$$

Since we want to express this relation in a form $\overline{\mathbf{D}}\mathbf{E}$, we have to write the current density $\mathbf{j}$ as a linear function of electric field. We can use the following relation

$$\mathbf{j} = \frac{\partial}{\partial t}\left(\mathbf{D} - \epsilon_0\mathbf{E}\right) = \frac{\partial}{\partial t}\left(\epsilon_0\overline{\epsilon}\mathbf{E} - \epsilon_0\mathbf{E}\right) \tag{1.5}$$

to get the general wave equation (1.4) in form

$$\nabla^2\mathbf{E} - \nabla\cdot(\nabla\mathbf{E}) - \mu_0\epsilon_0\overline{\epsilon}\frac{\partial^2\mathbf{E}}{\partial t^2} = 0. \tag{1.6}$$

In order to linearize the equation, we expand the total electric field to the first order $\mathbf{E} = \mathbf{E}_0 + \delta\mathbf{E}$ where $\mathbf{E}_0$ is background electric field and $\delta\mathbf{E}$ is perturbed field. Let us assume zero background field $\mathbf{E}_0$ and the perturbation

to be of the form of planar wave $\delta\mathbf{E}(t,\mathbf{x}) = \delta\mathbf{E}_a(\omega,\mathbf{k})\cdot\exp[i(\mathbf{kx}-\omega t)]$. Under these assumptions the equation (1.6) becomes

$$\left[\frac{k^2c^2}{\omega^2}\left(\frac{\overline{\mathbf{kk}}}{k^2}-\overline{\mathbf{I}}\right)+\overline{\epsilon}(\omega,\mathbf{k})\right]\delta\mathbf{E}_a(\omega,\mathbf{k})=0. \tag{1.7}$$

Non-trivial solution requires zero determinant of the equation

$$\mathrm{Det}\overline{\mathbf{D}} = \mathrm{Det}\left[\frac{k^2c^2}{\omega^2}\left(\frac{\overline{\mathbf{kk}}}{k^2}-\overline{\mathbf{I}}\right)+\overline{\epsilon}(\omega,\mathbf{k})\right]=0. \tag{1.8}$$

This equation is general dispersion relation of waves in the plasma. Properties of the plasma in interest are included in the dielectric tensor $\overline{\epsilon}(\omega,\mathbf{k})$. Its determination is main problem in solving the dispersion relation. Explicit form of $\overline{\mathbf{D}}$ for $\mathbf{k}=\left(k_\perp,0,k_\parallel\right)$ is

$$\overline{\mathbf{D}}(\omega,\mathbf{k}) = \begin{pmatrix} -N_\parallel^2+\epsilon_{xx} & \epsilon_{xy} & N_\perp N_\parallel+\epsilon_{xz} \\ \epsilon_{yx} & -N^2+\epsilon_{yy} & \epsilon_{yz} \\ N_\perp N_\parallel+\epsilon_{zx} & \epsilon_{zy} & -N_\perp^2+\epsilon_{zz} \end{pmatrix} \tag{1.9}$$

with perpendicular/parallel refractive index $N_{\perp,\parallel} = \frac{ck_{\perp,\parallel}}{\omega}$.

1.1.3 Dielectric tensor in magnetized plasma

The form of the dielectric tensor $\overline{\epsilon}(\omega,\mathbf{k})$ for magnetized plasma can be derived using the linearized Vlasov equation (1.3)

$$\left[\frac{\partial}{\partial t}+\mathbf{v}\nabla+\frac{q}{m}\left(\mathbf{v}\times\mathbf{B}_0\right)\nabla_v\right]\delta f(t,\mathbf{x},\mathbf{v}) = -\frac{q}{m}\left(\delta\mathbf{E}+\mathbf{v}\times\delta\mathbf{B}\right)\frac{\partial f_0(t,\mathbf{x},\mathbf{v})}{\partial\mathbf{v}}.$$

Since the operator on the left hand side is the total time derivative, the perturbation δf can be easily computed from this equation

$$\delta f(t,\mathbf{x},\mathbf{v}) = -\frac{q}{m}\int\limits_{-\infty}^{t} dt'\left(\delta\mathbf{E}(t')+\mathbf{v}(t')\times\delta\mathbf{B}(t')\right)\frac{\partial f_0(t',\mathbf{x},\mathbf{v})}{\partial\mathbf{v}}.$$

We transform the integration time with respect to the time in interest $\tau = t-t'$ and introduce plane waves once again: $\delta\mathbf{E}(t') = \delta\mathbf{E}_a(\omega,\mathbf{k})\cdot\mathrm{e}^{-i\varphi(\tau)}$ with the phase $\varphi(\tau) = \mathbf{k}[\mathbf{x}(t)-\mathbf{x}(t')]-\omega\tau$. The perturbed distribution function can be modified to the form

$$\delta f(t,\mathbf{x},\mathbf{v}) = -\frac{q}{m}\mathbf{M}(t)\delta\mathbf{E}_a(\omega,\mathbf{k}) \tag{1.10}$$

where the vector $\mathbf{M}$ is

$$\mathbf{M}(t) = \int_0^\infty d\tau \exp\left[-i\varphi(\tau)\right] \cdot \left[\left(1 - \frac{\mathbf{k}\mathbf{v}(t')}{\omega}\right)\nabla_v f_0 + \frac{1}{\omega}\left(\mathbf{k}\nabla_v f_0\right)\mathbf{v}(t')\right] \quad (1.11)$$

Knowledge of the perturbed distribution function allows to compute total perturbed current density

$$\delta\mathbf{j} = \sum_s \delta\mathbf{j}_s = \sum_s q_s \int d^3v \cdot \mathbf{v}\delta f_s$$

where the summation goes over all species contained in the plasma. We substitute for the perturbed distribution function from (1.10) to get

$$\delta\mathbf{j} = -\sum_s \frac{q_s^2}{m_s}\int d^3v \cdot \mathbf{v}\left(\mathbf{M}_s\delta\mathbf{E}_a\right) = -\sum_s \frac{q_s^2}{m_s}\int d^3v \cdot \left(\overline{\mathbf{v}\mathbf{M}_s}\right)\delta\mathbf{E}_a. \quad (1.12)$$

The equation (1.5) for planar waves is given as

$$\delta\mathbf{j} = -i\omega\epsilon_0\left(\overline{\epsilon} - 1\right)\delta\mathbf{E}_a. \quad (1.13)$$

One can compare equations (1.12) and (1.13) to find the relation for the dielectric tensor

$$\overline{\epsilon} = \overline{\mathbf{I}} - \sum_s \frac{i\omega_{ps}^2}{n_s\omega}\int d^3v \cdot \overline{\mathbf{v}\mathbf{M}_s}. \quad (1.14)$$

The integration over velocity space can be done in cylindrical coordinates $d^3v = v_\perp dv_\perp dv_\parallel d\psi$. The integration procedure over ψ and τ (in (1.11)) can be found in the book by Baumjohann and Treumann (1996). We present the resulting form given by Goldstein et al. (1985) which is slightly different from the form given by Baumjohann and Treumann (1996)

$$\overline{\epsilon}(\omega,\mathbf{k}) = \overline{\mathbf{I}} - \sum_s \frac{2\pi\omega_{p,s}^2}{n_{0,s}\omega^2}\int_0^\infty\int_{-\infty}^\infty dv_\perp dv_\parallel \cdot \left(\sum_{l=-\infty}^{l=+\infty}\frac{\mu_s}{\alpha_{l,s}}\cdot\overline{\mathbf{S}}_{l,s}(v_\parallel, v_\perp) + v_\parallel\nu_s \mathrm{e}_z\mathrm{e}_z\right) \quad (1.15)$$

where

$$\begin{aligned}\mu_s &= \omega\frac{\partial f_{0,s}}{\partial v_\perp} + k_\parallel v_\perp\frac{\partial f_{0,s}}{\partial v_\parallel} - k_\parallel v_\parallel\frac{\partial f_{0,s}}{\partial v_\perp}\\ \nu_s &= v_\parallel\frac{\partial f_{0,s}}{\partial v_\perp} - v_\perp\frac{\partial f_{0,s}}{\partial v_\parallel}\\ \alpha_{l,s} &= k_\parallel v_\parallel + l\omega_{c,s} - \omega\end{aligned} \quad (1.16)$$

and the tensor $\overline{\mathbf{S}}_{l,s}$ is defined as

$$\overline{\mathbf{S}}_{l,s} = \begin{pmatrix} \frac{l^2\omega_{c,s}^2}{k_\perp^2}J_l^2 & \frac{ilv_\perp\omega_{c,s}}{k_\perp}J_lJ_l' & \frac{lv_\parallel\omega_{c,s}}{k_\perp}J_l^2 \\ -\frac{ilv_\perp\omega_{c,s}}{k_\perp}J_lJ_l' & v_\perp^2 J_l'^2 & -iv_\parallel v_\perp J_lJ_l' \\ \frac{lv_\parallel\omega_{c,s}}{k_\perp}J_l^2 & iv_\parallel v_\perp J_lJ_l' & v_\parallel^2 J_l^2 \end{pmatrix}. \tag{1.17}$$

Here J_l denotes Bessel function of the l-th order of the argument $\xi = \frac{k_\perp v_\perp}{\omega_{c,s}}$ and J_l' is its derivative with respect to its argument. The form of the dielectrical tensor (1.15) holds for the plasma with distribution function $f_0(v_\perp, v_\parallel)$ which satisfies

$$\left(\frac{\partial f_0}{\partial v_x}, \frac{\partial f_0}{\partial v_y}, \frac{\partial f_0}{\partial v_z}\right) = \left(\frac{v_x}{v_\perp}\frac{\partial f_0}{\partial v_\perp}, \frac{v_y}{v_\perp}\frac{\partial f_0}{\partial v_\perp}, \frac{\partial f_0}{\partial v_\parallel}\right),$$

where $v_\perp = \sqrt{v_x^2 + v_y^2}$ and $v_\parallel = v_z$. In order to perform the integration over $v_\perp$ and $v_\parallel$, one must specify the form of the distribution function $f_{0,s}$. In the case of bi-Maxwellian plasma the distribution function has form

$$f_{0,s}(v_\perp, v_\parallel) = \frac{n_s}{\pi^{3/2}v_{t\perp,s}^2 v_{t\parallel,s}} \exp\left(-\frac{v_\perp^2}{v_{t\perp,s}^2} - \frac{v_\parallel^2}{v_{t,\parallel}^2}\right) \tag{1.18}$$

where $v_{t\perp,\parallel}^2 = 2k_BT_{\perp,\parallel}/m_s$ is squared perpendicular/parallel thermal velocity and $T_{\perp,\parallel}$ is perpendicular/parallel temperature.

The integration procedure is given by Baumjohann and Treumann (1996) or Goldstein et al. (1985) and the result is

$$\overline{\epsilon}(\omega, \mathbf{k}) = \overline{\mathbf{I}} + \sum_s \overline{\mathbf{Q}}_s \tag{1.19}$$

where the tensor $\overline{\mathbf{Q}}_s$ has components

$$\begin{aligned} Q_{xx,s} &= \frac{\omega_{p,s}^2}{\omega^2}\sum_l \frac{l^2\Lambda_l(\lambda_s)}{\lambda_s}\left[A_s - 1 + A_s\kappa_{l,s}Z(\zeta_{l,s})\right], \\ Q_{xy,s} &= i\frac{\omega_{p,s}^2}{\omega^2}\sum_l l\Lambda_l'(\lambda_s)\left[A_s - 1 + A_s\kappa_{l,s}Z(\zeta_{l,s})\right], \\ Q_{xz,s} &= \frac{\omega_{p,s}^2}{\omega^2}\frac{v_{t\parallel,s}k_\perp}{\omega_{c,s}}A_s\sum_l \frac{l\Lambda_l(\lambda_s)}{\lambda_s}\left[\kappa_{l,s} + \kappa_{l,s}\zeta_{l,s}Z(\zeta_{l,s})\right], \\ Q_{yx,s} &= -Q_{xy,s}, \end{aligned} \tag{1.20}$$

$$
\begin{aligned}
Q_{yy,s} &= \frac{\omega_{p,s}^2}{\omega^2}\sum_l \left(\frac{l^2\Lambda_l(\lambda_s)}{\lambda_s} - 2\lambda_s\Lambda_l'(\lambda_s)\right)\left[A_s - 1 + A_s\kappa_{l,s}Z(\zeta_{l,s})\right], \\
Q_{yz,s} &= -i\frac{\omega_{p,s}^2}{\omega^2}\frac{v_{t\parallel,s}k_\perp}{\omega_{c,s}}A_s\sum_l \Lambda_l'(\lambda_s)\left[\kappa_{l,s} + \kappa_{l,s}\zeta_{l,s}Z(\zeta_{l,s})\right], \\
Q_{zx,s} &= Q_{xz,s}, \\
Q_{zy,s} &= -Q_{yz,s}, \\
Q_{zz,s} &= 2\frac{\omega_{p,s}^2}{\omega^2}\sum_l \Lambda_l(\lambda_s)\left[\kappa_{l,s}\zeta_{l,s} + \kappa_{l,s}\zeta_{l,s}^2 Z(\zeta_{l,s})\right].
\end{aligned}
$$

In the tensor components, $A_s = \frac{v_{t\perp,s}^2}{v_{t\parallel,s}^2} = \frac{T_{\perp,s}}{T_{\parallel,s}}$ is temperature anisotropy of the species s and λ_s, $\kappa_{l,s}$, $\zeta_{l,s}$ are defined by relations

$$
\begin{aligned}
\lambda_s &= \frac{v_{t\perp,s}^2 k_\perp^2}{2\omega_{c,s}^2}, \\
\kappa_{l,s} &= \frac{\omega - (1 - 1/A_s)\, l\omega_{c,s}}{v_{t\parallel,s}k_\parallel}, \\
\zeta_{l,s} &= \frac{\omega - l\omega_{c,s}}{v_{t\parallel,s}k_\parallel}.
\end{aligned}
\tag{1.21}
$$

$Z(\zeta)$ is the Fried-Conte plasma dispersion function

$$
Z(\zeta) = \frac{1}{\sqrt{\pi}}\int_{-\infty}^{+\infty}\frac{\exp\left(-z^2\right)}{z-\zeta}dz
$$

and $\Lambda_l(\lambda) = \exp(-\lambda)I_l(\lambda)$ where I_l is the modified Bessel function of the order l and Λ_l' denotes derivative with respect to argument λ.

1.2 Temperature anisotropy driven instabilities

1.2.1 Mirror instability

Mirror instability (MI) is driven mainly in the high β plasma in regions where the perpendicular temperature exceeds the parallel: $T_\perp > T_\parallel$. It can be

showed (Hasegawa (1969)) that in such case the kinetic pressure perturbance is in antiphase to the magnetic field perturbance and that the change of total perpendicular pressure (perpendicular kinetic and magnetic) of the multi-species plasma with cold electrons is negative if plasma parameters fulfil relation

$$\Gamma = \sum_s \beta_{\perp,s} \left(A_s - 1\right) - 1 > 0. \tag{1.22}$$

Relation $\Gamma = 0$ is a threshold of the mirror instability.

A traditional picture of the linear instability is following: if the perpendicular plasma beta $\beta_{\perp,s}$ and temperature anisotropy A_s are such that the relation (1.22) is satisfied, the total perpendicular pressure decreases when the field is increased and magnetic field lines are then compressed by the plasma from neighbouring regions. The magnetic field is thus increased and the whole process can repeat until the plasma stabilizes. Hasegawa (1969) shows that the change of the parallel pressure is lower than the change of the perpendicular pressure and the instability thus leads naturally to the decrease of temperature anisotropy.

Southwood and Kivelson (1993) emphasize the importance of particles with low parallel velocity which are resonant with the field. These particles behave in a different way than the bulk plasma because their pressure perturbance is in the phase with the field perturbance. Southwood and Kivelson (1993) note that these resonant particles distinguish results obtained from the kinetic approach and fluid approach. The fluid approach yields the same instability condition of the mirror mode (1.22) but different dispersion relation.

The determination of mirror mode properties requires solution of the dispersion relation (1.8) with the magnetized dielectrical tensor (1.19). This problem can be solved analytically under the assumption that the ϵ_{xy} component of the dielectrical tensor (1.19) vanishes in the limit of low-frequency long-wavelength waves (e.g., Hasegawa (1969), Treumann and Baumjohann (1997)):

$$\begin{aligned} \frac{|\omega|}{\omega_{c,s}} &\ll 1, \\ \frac{v_{t\perp,s} k_\perp}{\omega_{c,s}} &\ll 1, \\ \frac{v_{t\parallel,s} k_\parallel}{\omega_{c,s}} &\ll 1. \end{aligned} \tag{1.23}$$

This simplification can be explained as follows: since $\omega \ll \omega_{c,s}$, $\kappa_{l,s}$ and $\zeta_{l,s}$ from (1.21) satisfy relations $\kappa_{l,s} \approx -\kappa_{-l,s}$ and $\zeta_{l,s} \approx -\zeta_{-l,s}$. Moreover,

$Z(\zeta_{l,s}) \approx -Z(\zeta_{-l,s})$ in the limit $|\zeta_{l,s}| \gg 1$ and $\Lambda_l(\lambda_s) = \Lambda_{-l}(\lambda_s)$ for all λ_s. One can conclude that each l term of the sum in Q_{xy} in (1.20) cancels with the $-l$ term. The $l = 0$ term of Q_{xy} is equal to zero. For the same reasons the l and $-l$ terms cancel in the component Q_{yz}, however, this component has nonzero $l = 0$ term. All the other components of $\overline{\mathbf{Q}}_s$ have l and $-l$ terms of the same sign.

Using the assumption $\epsilon_{xy} = 0$, the dispersion relation of mirror waves in cold electrons plasma is usually written as

$$\epsilon_{yy} = 1 + \sum_s Q_{yy,s} = \frac{k^2 c^2}{\omega^2} \tag{1.24}$$

where $Q_{yy,s}$ is defined in (1.20). Solution to this equation with respect to the growth rate is (Hellinger (2007))

$$\gamma_{mi} = \frac{k_\parallel}{\sqrt{\pi}} \tilde{v} \left(\Gamma - \frac{3}{4} k_\perp^2 \tilde{r}^2 - \frac{k_\parallel^2}{k_\perp^2} \Pi \right) \tag{1.25}$$

where

$$\tilde{v}^{-1} = \sum_s \frac{\beta_{\perp,s} A_s}{v_{t\parallel,s}},$$

$$\tilde{r}^2 = \sum_s \beta_{\perp,s} \left(A_s - 1 \right) r_{c,s}^2,$$

$$r_{c,s} = \frac{v_{t\perp,s}}{\omega_{c,s}},$$

$$\Pi = 1 + \frac{1}{2} \sum_s \left(\beta_{\perp,s} - \beta_{\parallel,s} \right)$$

and Γ is given in (1.22). It is assumed $k_\perp \to 0$ and $k_\parallel / k_\perp \to 0$ near the threshold and the mirror mode becomes unstable (has a positive growth rate) for $\Gamma > 0$. Mirror mode has zero real part of the frequency.

Hasegawa (1969) showed that in the case of inhomogenous one ion population cold electrons plasma the mirror mode has non-zero real part of the frequency equal to the frequency of ion drift wave $\omega_r = \omega_{d,\mathrm{i}} = \frac{\kappa k_\perp v_{t\parallel,\mathrm{i}}^2}{\omega_{c,\mathrm{i}}}$ where κ is the field gradient in the perpendicular direction. This result was revisited by Hellinger (2008) to the form

$$\omega_r = \left[\frac{3}{2} \left(A_\mathrm{i} - 1 \right) - \frac{2}{\beta_{\perp,\mathrm{i}}} \right] \omega_{d,\mathrm{i}}.$$

Mirror instability in the inhomogenous plasma is called *drift mirror instability*. Hasegawa (1969) also derived that the instability condition (1.22)

and the growth rate (1.25) remains unchanged in the inhomogenous plasma. However, Hellinger (2008) notes that the instability condition (1.22) is not correct for the drift mirror instability and that no simple threshold condition can be derived.

Mirror waves are linearly polarized nonpropagating and are characterized by the anticorrelation between fluctuations of plasma pressure and magnetic pressure. In other words, fluctuations of magnetic field magnitude and plasma density are anticorrelated in mirror structures. This anticorrelation is important identifier of mirror waves. Mirror structures have been observed in Earth's (Hill et al. (1995), Génot et al. (2009)) and Jupiter's magnetosheaths (Joy et al. (2006)), in the solar wind (Winterhalter et al. (1994)) or at Io (Russell et al. (1999a), Russell et al. (1999b)).

1.2.2 Ion cyclotron instability

Ion cyclotron instability (ICI) is driven by the temperature anisotropy of ions and excites parallel propagating electromagnetic waves. It is an analogy of the whistler instability which is driven by the temperature anisotropy of electrons. ICI results from the resonant cyclotron interaction of the field with rotating ions and has a left handed circular polarization and frequency $\omega_r \lesssim \omega_{c,\mathrm{i}}$.

Let us assume purely parallel propagating mode $\mathbf{k} \times \mathbf{B}_0 = 0$, i.e., $k_\perp = 0$. In such case components ϵ_{xz} and ϵ_{yz} of the dielectrical tensor (1.19) vanish and components ϵ_{xx} and ϵ_{yy} are identical (see (1.20)). The dispersion relation (1.8) can be then written as

$$\epsilon_{zz}\left(D_{xx}^2 + D_{xy}^2\right) = 0.$$

This relation contains two modes: relation $\epsilon_{zz} = 0$ is a dispersion relation of electrostatic longitudinal oscillations while the round bracket is a dispersion relation of parallel propagating electromagnetic waves. We are interested in the latter one.

Roots of the round bracket are given by the equation

$$D_{xx} = \pm i D_{xy} \tag{1.26}$$

which is satisfied for two independent modes denoted by the sign $\pm$ on the right-hand side. These two modes are left-handed and right-handed polarized parallel propagating electromagnetic waves. The dispersion relation (1.26) is determinant representation of equation

$$\begin{pmatrix} D_{xx} & D_{xy} \\ -D_{xy} & D_{xx} \end{pmatrix} \begin{pmatrix} \delta E_x \\ \delta E_y \end{pmatrix} = 0.$$

We can substitute $D_{xx} = \pm iD_{xy}$ and rewrite this equation to the form containing both polarizations

$$\begin{pmatrix} D_R & 0 \\ 0 & D_L \end{pmatrix} \begin{pmatrix} \delta E_R \\ \delta E_L \end{pmatrix} = 0$$

where $\delta E_{R,L} = \delta E_x \mp i\delta E_y$ and

$$D_{R,L} = D_{xx} \pm iD_{xy} = -N_\parallel^2 + \epsilon_{xx} \pm i\epsilon_{xy}. \tag{1.27}$$

R symbol denotes right-handed polarized electromagnetic wave whose electric field vector rotates around the background magnetic field $\mathbf{B}_0$ in the same sense as particles with negative charge. Left-handed polarized waves (L) have the electric field vector rotating in the same sense as positive ions and can be excited by the ion cyclotron instability.

For $k_\perp = 0$, i.e., $\lambda_s = 0$, only $l = 1$ and $l = -1$ terms of sums in Q_{xx} and Q_{xy} in (1.20) survive and the dispersion relation $D_{R,L}$ (1.27) becomes

$$D_{R,L}(\omega, \mathbf{k}) = \omega^2 - k_\parallel^2 c^2 + \sum_s \omega_{p,s}^2 (A_s - 1) + \sum_s \omega_{p,s}^2 A_s \kappa_{\mp 1,s} Z(\zeta_{\mp 1,s}) = 0. \tag{1.28}$$

Note that, even though we have stated that the ion cyclotron instability is driven by positive ions, the dispersion relation $D_{ICI} = D_L$ (1.28) contains all plasma species including electrons and other negative ions.

Consider plasma composed of electrons and one ionic species. The contribution of electrons can be converted using the large argument ($|\zeta_{1,\mathrm{e}}| \gg 1$) expansion of the plasma dispersion function to the form

$$\omega_{p,\mathrm{e}}^2 (A_\mathrm{e} - 1 + A_\mathrm{e} \kappa_{1,\mathrm{e}} Z(\zeta_{1,\mathrm{e}})) \approx -\omega_{p,\mathrm{e}}^2 \left(1 + \frac{\omega_{c,\mathrm{e}}}{\omega - \omega_{c,\mathrm{e}}}\right).$$

This contribution is negligible in limit $|\omega| \ll |\omega_{c,\mathrm{e}}|$. The contribution of ions can not be easily treated analytically because $|\zeta_{1,\mathrm{i}}| \gtrsim 1$ and neither large argument expansion nor small argument expansion of the dispersion function can be used. Gary (1993) shows that weak growth/damping rate $|\gamma| \ll |\omega_r|$ of right- and left-handed electromagnetic modes driven by temperature anisotropy of ions is given as

$$\gamma_{R,L} = \frac{\sqrt{\pi}}{2\omega_r} \frac{\omega_{p,\mathrm{i}}^2}{v_{t\parallel,\mathrm{i}} k_\parallel} \left[-A_\mathrm{i}\omega_r \pm (1 - A_\mathrm{i})\,\omega_{c,\mathrm{i}}\right] \exp\left[\frac{(\omega_r \pm \omega_{c,\mathrm{i}})^2}{v_{t\parallel,\mathrm{i}}^2 k_\parallel^2}\right] \tag{1.29}$$

for $k_\parallel > 0$. Ions with $\omega_{c,\mathrm{i}} > 0$ can drive the left-handed ion cyclotron instability ($\gamma_{ICI} = \gamma_L > 0$) in the frequency region $\omega_r < \omega_{c,\mathrm{i}}$ whenever

$$A_\mathrm{i} = \frac{T_{\perp,\mathrm{i}}}{T_{\parallel,\mathrm{i}}} > -\frac{\omega_{c,\mathrm{i}}}{\omega_r - \omega_{c,\mathrm{i}}} > 1.$$

The anisotropy serves as a source of free energy necessary for development of the instability: $\gamma_{R,L}$ from (1.29) is always negative for isotropic plasma with $A_\mathrm{i} = 1$. The resonance condition (1.16) $k_\parallel v_\parallel + \omega_{c,\mathrm{i}} - \omega = 0$ implies that resonant ions are those which move in the opposite direction to the wave.

Proton cyclotron waves have been detected in the Earth's magnetosheath (Anderson and Fuselier (1993)) or in the fast solar wind (Gary et al. (2001)). In both cases, the waves were present in a low-beta plasma ($\beta_{\parallel,\mathrm{p}} < 1$) and manifested constraints of the maximum proton temperature anisotropy $T_{\perp,\mathrm{p}}/T_{\parallel,\mathrm{p}}$ of the form

$$\frac{T_{\perp,\mathrm{p}}}{T_{\parallel,\mathrm{p}}} - 1 = \frac{S}{\beta^{\alpha}_{\parallel,\mathrm{p}}} \tag{1.30}$$

with S, α both positive. Such dependence of anisotropy on beta can be derived from linear Vlasov theory (Gary and Lee (1994)).

Cyclotron waves of heavier ions have been observed in the magnetosphere of Saturn (Russell et al. (2006)) or at Io (Russell et al. (2003b)).

1.2.3 Parallel fire hose instability

A plasma with anisotropic ions can drive also right-handed polarized waves of frequency $\omega_r < \omega_{c,\mathrm{i}}$. It is easy to show that the growth rate of right-handed polarized waves γ_R (1.29) is positive whenever

$$A_\mathrm{i} = \frac{T_{\perp,\mathrm{i}}}{T_{\parallel,\mathrm{i}}} < \frac{\omega_{c,\mathrm{i}}}{\omega_r + \omega_{c,\mathrm{i}}} < 1.$$

In this case the resonance condition (1.16) $k_\parallel v_\parallel - \omega_{c,\mathrm{i}} - \omega = 0$ yields that ions moving in the same direction as the wave are resonant. This instability is called parallel fire hose instability (PFI). It can be treated in the fluid approach and can be described as follows: let the plasma flows along the magnetic field direction in the flux tube, when the flux tube is bent from the parallel direction, the parallel pressure force acts to increase the perturbance while the perpendicular pressure force and magnetic tension force act to restore the flux tube to the unperturbed shape. The instability evolves when the parallel pressure force exceeds the restoring forces. This simple condition yields instability criterion of the parallel fire hose instability

$$\Delta = \beta_\parallel - \beta_\perp > 2.$$

This fluid threshold predicts that the parallel fire hose can evolve only in moderate or high parallel beta plasma $\beta_\parallel \geq 2$. The kinetic approach lowers this limit but it still holds that the parallel fire hose instability can not

develop in low-beta plasma. No such limit exists for $A_\mathrm{i} > 1$ instabilities, i.e., mirror and ion cyclotron modes.

Parallel kinetic dispersion relation of the ion parallel fire hose instability is given by the right-handed dispersion relation D_R (1.28)

$$D_{PFI}(\omega, \mathbf{k}) = \omega^2 - k_\parallel^2 c^2 + \sum_s \omega_{p,s}^2 (A_s - 1) + \sum_s \omega_{p,s}^2 A_s \kappa_{-1,s} Z(\zeta_{-1,s}) = 0.$$

The contribution of electrons can be neglected as in the case of the ion cyclotron instability because $|\zeta_{-1,\mathrm{e}}| \gg 1$.

Linear Vlasov theory predicts a threshold of the parallel fire hose of the form (1.30) with $S < 0$ (Gary et al. (1998)). Kasper et al. (2002) observed constraint of the temperature anisotropy of that form in the solar wind and attributed it to the growth of the parallel fire hose instability. However, they did not consider the oblique fire hose instability which has similar threshold. Hellinger et al. (2006) solved dispersion relations of both fire hoses and showed that the measured temperature anisotropy constraint corresponds rather to the oblique fire hose instability. Moreover, Bale et al. (2009) showed that fluctuations of the magnetic field are enhanced along the threshold of oblique fire hose instability.

1.2.4 Oblique fire hose instability

Hellinger and Matsumoto (2000) found that there is additional kinetic instability in the anisotropic plasma with $T_\parallel > T_\perp$. As in the case of PFI, this instability exists only in moderate and high-parallel beta plasma. This instability has maximum growth rate at oblique angles to the ambient magnetic field and is therefore called oblique fire hose instability (OFI). It has other properties similar to those of the mirror mode; OFI has zero real frequency and anticorrelated fluctuating magnetic field and density.

In contrast to the parallel fire hose, the oblique fire hose evolves in nonlinear manner. The parallel fire hose grows to modest level of fluctuations and then saturates. During this process the temperature anisotropy is slightly increased and then remains constant. The oblique fire hose grows rapidly to high level of fluctuations at the beginning. Then the oblique fire hose instability excites Alfvén waves which are strongly damped. During this damping, the anisotropy A_i increases (tends to $A_\mathrm{i} = 1$). The oblique fire hose is very efficient in increasing the anisotropy.

There is evidence that OFI is active in the solar wind and plays role in constraining the temperature anisotropy (see section 1.2.3).

1.2.5 Comparison of temperature anisotropy driven instabilities

We have described four instabilities which are driven by the temperature anisotropy of ions in previous sections. Table 1.1 gives a brief summary of their properties. One can find a kind of symmetry between instabilities; MI has the same properties as OFI except that they need different anisotropy and thus can not coexist in the plasma. The same holds for the ICI and PFI. Instabilities of the same anisotropy can naturally coexist in the plasma and compete for the free energy in the system.

Instability	Anisotropy	Frequency	Maximum γ at	Polarization
MI	$A_\mathrm{i} > 1$	$\omega_r = 0$	$\mathbf{k} \times \mathbf{B}_0 \neq 0$	linear
ICI	$A_\mathrm{i} > 1$	$\omega_r < \omega_{c,\mathrm{i}}$	$\mathbf{k} \times \mathbf{B}_0 = 0$	left-handed
PFI	$A_\mathrm{i} < 1$	$\omega_r < \omega_{c,\mathrm{i}}$	$\mathbf{k} \times \mathbf{B}_0 = 0$	right-handed
OFI	$A_\mathrm{i} < 1$	$\omega_r = 0$	$\mathbf{k} \times \mathbf{B}_0 \neq 0$	linear

Table 1.1: Basic properties of mirror (MI), ion cyclotron (ICI), parallel (PFI) and oblique fire hose (OFI) instabilities.

Mirror structures are often observed with high amplitude of fluctuating field $\delta B/B \gtrsim 0.1$. This fact indicates the nonlinear evolution of the mirror instability. The oblique fire hose has also nonlinear evolution. On the contrary, ion cyclotron and parallel fire hose instabilities have rather linear evolution.

Figure 1.1 shows isocontours of maximum growth rate of temperature anisotropy driven instabilities in $\beta_{\parallel,\mathrm{i}} - A_\mathrm{i}$ space. Growth rates are computed from the linear Vlasov theory for the plasma composed of isotropic electrons and anisotropic bi-Maxwellian ions of mass $m_\mathrm{i} = 22 m_\mathrm{p}$ where m_p is the proton mass. The lines correspond to the particular instabilities as follows: solid - ICI, dotted - MI, dashed - PFI, dash-dotted - OFI. Numbers a on the lines denote the value of growth rate γ in unit of cyclotron frequency $\gamma = a\omega_{c,\mathrm{i}}$.

Evidently, the distance of ions from the isotropy is anticorrelated to the parallel beta for all the instabilities. Hellinger et al. (2006) have showed that, for electron-proton plasma, thresholds of these instabilities can be expressed in the form

$$\frac{T_{\perp,\mathrm{p}}}{T_{\parallel,\mathrm{p}}} - 1 = \frac{S}{\left(\beta_{\parallel,\mathrm{p}} - \beta_0\right)^\alpha}.$$

Instabilities operating in $T_{\perp,\mathrm{p}}/T_{\parallel,\mathrm{p}} > 1$ plasma (MI and ICI) have $S > 0$ and negligible β_0 while both fire hoses have negative S and non-negligible β_0.

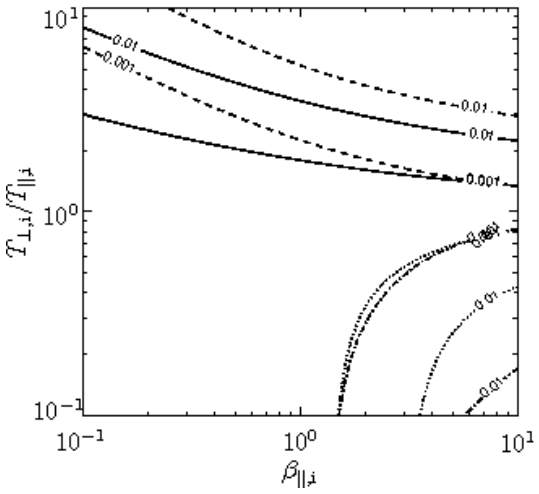

Figure 1.1: Isocontours of maximum growth rate of temperature anisotropy driven instabilities as predicted by linear Vlasov theory for anisotropic ions of mass $m_\mathrm{i} = 22\ m_\mathrm{p}$ and isotropic electrons. The lines correspond to the growth rates of ICI - solid, MI - dashed, PFI - dotted, OFI - dash-dotted.

It can be seen that in the low-beta plasma ICI has larger growth rate than MI. This feature holds for the electron-proton plasma as well (Gary et al. (1993)). Similarly, the parallel fire hose has larger growth rate than the oblique fire hose, thus parallel modes have dominant growth rates in the low-beta electron-one ionic species plasma. However, there is evidence that the oblique modes can grow to significant level even in regions where the linear theory predicts the parallel modes to dominate (e.g., measurements of solar wind: Hellinger et al. (2006), Bale et al. (2009)).

One of possible explanations is that mirror and oblique fire hose modes are nonpropagating in the reference frame of plasma while ion cyclotron and parallel fire hose modes propagate fast along the magnetic field. Other reason can be in the fact that real space plasmas are not always bi-Maxwellian. For example, the pickup process produces ring-type distribution function with anisotropy $A > 1$ and the plasma with such distribution function behave differently. This problem is not well inspected.

The growth of instabilities is also affected by the composition of the plasma which is not purely electron-proton in the case of solar wind, there is a small density of alpha particles. Numerical simulations of Price et al. (1986) or Gary et al. (1993) showed that an introduction of alpha particles significantly reduces the growth rate of ICI and thus decreases the region

where the ICI is dominant. For example, the results of Gary et al. (1993) show that ICI dominates in electron-proton plasma for $\beta_{\parallel,\mathrm{p}} \lesssim 6$, but addition of alpha particles of density $n_\alpha = 0.03 n_\mathrm{p}$ limits the region of dominant ICI to $\beta_{\parallel,\mathrm{p}} \lesssim 1$.

Each component of the multi-species plasma tends to drive ion cyclotron wave with frequency corresponding to its specific cyclotron frequency. On the other hand, the mirror mode is fed by all components in the multi-species plasma. Consequently the growth rates of particular ion cyclotron modes can drop below the growth rate of mirror mode. Mirror structures observed at Io in the very low beta evolved probably due to this effect (Huddleston et al. (1999)).

Simulations of McKean et al. (1992) show that recyclation of anisotropic ions can support the dominance of mirror mode. The anisotropy of ions was externally maintained on the constant value in these simulations. This effect was included to simulate an ongoing compression of the plasma in magnetosheath. Results show that this recyclation increases the growth rate of the MI while it damps the ICI. The pick-up process can be considered to be similar recycling process because it increases the anisotropy of the distribution function. The effect of pick-up process on the growth rates of $A_s > 1$ instabilities is not well examined.

Chapter 2

Plasma environment of Io

Jupiter's moon Io was discovered by Galileo Galilei in 1610 and is one of four Galilean moons. With the radius $R_{Io} = 1821$ km, Io is the third largest Galilean moon and the fourth largest moon in the solar system. Io, being the innermost of the Galilean moons, orbits Jupiter at distance $R_{orbit} \approx 6$ R_J with 42 hours period, here $R_J \doteq 71500$ km is radius of the Jupiter. Io is deeply immersed in the Jovian massive magnetosphere, the magnetic field at Io's orbit is about $B_J = 1800$ nT. Io has atmosphere and ionosphere which interact strongly with the Jupiter's magnetospheric plasma.

2.1 Ionian atmosphere

Io has strong volcanic activity, there are more than 400 active volcanoes on the surface of Io. The volcanism has been discovered by *Voyager 1* during its Jupiter flyby in 1979 (Morabito et al. (1979), Strom et al. (1979)). Peale et al. (1979) found that the volcanism is caused by the interaction with other Galilean moons, Europa and Ganymede. Particles eructed from the volcanoes together with those sublimated from surface frosts form Io's neutral atmosphere. The atmosphere is patchy, the local source rate depends on the frost distribution and proximity of volcanoes. It is also significantly temporally varying as the density source rate depends on the actual volcanic activity and position of Io with respect to the Sun which affects the frost sublimation.

The question which of the atmosphere sources is dominant is currently unresolved. Saur and Strobel (2004) modeled the collapse of the sublimation driven part of the atmosphere during solar eclipse and its influence on the far-ultraviolet radiation power. From the comparison with *Hubble Space Telescope* (HST) observations, they concluded that the sublimation driven

contribution exceeds the volcanic contribution by one order during sunlight. Jessup et al. (2004) analyzed HST observations of the *Prometheus* plume and reported smooth decrease of density apart from the plume leading also to the conclusion that the contribution of frost sublimation dominates. However, there are also measurements that predicate the atmosphere driven rather by the volcanic activity (Spencer et al. (2005)). Recently, Walker et al. (2010) and Gratiy et al. (2010) developed a complex 3-D model for simulation of the neutral atmosphere, they included inhomogenous frost map and several volcanic plumes to the model. Their results are in good accordance with densities inferred from HST spectroscopic observations. Better match with observations was obtained with the composite atmosphere (including the volcanoes). The volcanic contribution is important mainly on the anti-Jovian hemisphere.

Although neutral sodium has been observed first at Io (Brown (1974)), main constituents are sulfur dioxide, firstly detected by Pearl et al. (1979), and sulfur oxide. Other components, such as S_2, S_3 and S_4, have been reported (Spencer et al. (2000)).

Io's atmosphere has a scale height about $H_{atm} \approx 100$ km $\approx 0.06 R_{Io}$ but neutral clouds extend up to $5.8 R_{Io}$ or further (e.g., Frank and Paterson (2001a)). This distance corresponds to the radius of the Hill sphere which is defined as a region where the attraction of Io exceeds the attraction of Jupiter. The atmosphere is asymmetric; it has larger scale height on the downstream side due to the drag force of the plasma and it has a day-night asymmetry. It has been found by Smyth and Wong (2004) that SO_2 density is dominant on the day side but decreases on the night side and can drop below densities of other constituents.

Atmospheric particles can be ionized in several processes such as electron impact ionization, photoionization and charge exchange ionization. Total ionization rate at Io is of the order of $10^{27} - 10^{28}$ ions per second (Bagenal (1997), Saur et al. (2003)). Huddleston et al. (1998) inferred the SO_2^+ ion production rate to be $8 \cdot 10^{26}$ ions per second. Hinson et al. (1998) evaluated ionosphere density profiles from *Galileo* radio measurements, the maximal electron density observed was $n_e = 277000$ cm^{-3}.

2.2 Plasma torus

Io's atmosphere and ionosphere lose about 1-3 ton of mass per second, about 20 % of it is in the form of ionized particles (Saur et al. (2003)). Escaped ionized particles maintain Io's plasma torus, a torus shaped cloud of plasma that encircles Jupiter. The torus plasma is coupled to the Jupiter by magnetic

field aligned currents, this coupling forces the torus to corotate the Jupiter with its rotation velocity. The torus velocity at Io is $V_{torus} = 74$ km.s^{-1} (Frank and Paterson (2001b)). Io orbits with velocity $V_{Io} = 17$ km.s^{-1} only so the torus flows past Io with relative velocity $V_{rel} = 57$ km.s^{-1} $= 0.3V_A$ where V_A is the torus plasma Alfvén velocity. Fresh plasma is accelerated to the torus bulk speed.

Most of our knowledge of torus plasma properties comes from in-situ measurements of *Voyager 1* which flew by Jupiter in March 1979, *Galileo* which orbited Jupiter from 1995 to 2003 and *Cassini* which flew by at the turn of 2000 and 2001. Onboard instruments provided information about torus plasma composition, density and temperature.

Bagenal (1994) analyzed data obtained from *Plasma Science* and *Ultraviolet Spectrometer* instruments on the *Voyager 1* and Stefflet al. (2004) analyzed the data from *Ultraviolet Imaging Spectrometer* on board of the *Cassini*. They examined torus plasma composition and its radial profile on the equatorial plane of Jupiter in the range $(6, 9)$ R_J, their results slightly differ. The torus contains mainly atomic ions of O^+, S^+ and S^{++} and to the lower extent the ions of O^{++}, S^{3+} and S^{4+}. Relative concentrations of dominant species at Io's orbital distance $R_{orbit} \approx 6R_J$ are presented in the following table for both observations together with average ionic charge $\langle Z \rangle$ and mass $\langle A \rangle$ and ratio of oxygen to sulfur O/S. The torus does not contain molecular ions in a large degree because molecules rapidly dissociate. Density of SO_2^+ is estimated to be bellow 2 % (Bagenal (1994), Warnecke et al. (1997)).

$[O^+]$	$[O^{++}]$	$[S^+]$	$[S^{++}]$	$[S^{3+}]$	$[S^{4+}]$	$\langle Z \rangle$	$\langle A \rangle$	O/S	Source
0.40	0.01	0.10	0.17	0.02	-	1.3	22.6	1.4	*Vo.*
0.22	0.03	0.07	0.21	0.03	0.03	1.7	25.2	0.7	*Ca.*

Table 2.1: Densities of particular ionic species at Io's orbital distance (given in n_e) and average charge (in electron charge), mass (in proton mass) and ratio of oxygen to sulfur for given composition. The first row presents data from *Voyager 1* analyzed by Bagenal (1994), the second row contains data from *Cassini* analyzed by Stefflet al. (2004), in both papers see Figure 7.

These results imply significant temporal variability of torus properties which is ascribed to the variability of the source at Io. Delamere and Bagenal (2003) developed a numerical model to study the torus plasma properties in dependence on the parameters of the neutral source. They included charge exchange chemistry of neutral and ionized oxygen and sulphur. They obtained the source rate in the range $S_n = 0.6 - 2.4$ t.s^{-1} and the oxygen to

sulphur ratio in the range O/S $= 1.7 - 4.0$ to best fit the observations of *Voyager 1,2* and *Cassini* spacecrafts.

The electron density estimated by Bagenal (1994) is about $n_\mathrm{e} = 2000$ cm^{-3}. This result is similar to that obtained by Steffl et al. (2004). This density multiplied by the sum of relative densities from Table 2.1 gives ionic densities $n_\mathrm{i} = 1400$ cm^{-3} for *Voyager 1* and $n_\mathrm{i} = 1200$ cm^{-3} for *Cassini*. Crary et al. (1998) analyzed the data from *Galileo* to get the value of electron density $n_\mathrm{e} = 3800$ cm^{-3} and total ionic density of four major species in the range $n_\mathrm{i} = 2400 - 3900$ cm^{-3}. Ionic density inferred by Frank and Paterson (2001b) from *Galileo*'s observations vary in the range $n_\mathrm{i} = 1000 - 3000$ cm^{-3}.

Torus electron temperature at Io is about $T_\mathrm{e} = 5 - 6$ eV (Sittler and Strobel (1987), Bagenal (1994), Steffl et al. (2004)). Ionic temperatures are much higher: Bagenal (1994) obtained $T_\mathrm{i} = 60$ eV, Frank and Paterson (2001b) obtained $T_\mathrm{i} = 70$ eV and Crary et al. (1998) estimated the temperature of various species varying in range $T_\mathrm{i} = 10 - 55$ eV.

We give the overview of ranges of torus plasma parameters in the following table and we include ranges of other inferred parameters such as kinetic pressure p_s, kinetic to magnetic pressure ratio β_s and mean Larmor radius $r_{L,s}$ given by relations

$$\begin{aligned} p_s &= n_s k_B T_s, \\ \beta_s &= \frac{2\mu_0 p_s}{B_J^2}, \\ r_{L,s} &= \frac{m_s}{q_s B_J}\sqrt{\frac{8 k_B T_{\perp,s}}{\pi m_s}}. \end{aligned} \tag{2.1}$$

In the calculation of Larmor radius, we assume the torus plasma to be isotropic (i.e., $T_{\perp,s} = T_s$) and we take the ionic charge q_i and mass m_i as average of values from rows in Table 2.1. Jovian magnetic field at Io is $B_J = 1800$ nT.

	n [cm^{-3}]	T [eV]	p [nPa]	β [-]	r_L [km]
Electrons	2000-3800	5-6	1.6-3.7	0.0012-0.0029	0.005
Ions	1000-3900	10-70	1.6-43.7	0.001-0.034	4.4-11.6

Table 2.2: Torus plasma parameters: densities and temperatures were measured in-situ, other parameters are computed from relations (2.1). For the calculation of β and r_L we take the Jovian magnetic field $B_J = 1800$ nT and the ionic charge and mass as average of values in Table 2.1: $q_\mathrm{i} = 1.5e$ and $m_\mathrm{i} = 23.9 m_\mathrm{p}$.

2.3 Plasma torus interaction with Io

The plasma torus is significantly disturbed by presence of Io which changes local torus density, momentum and energy. The interaction is very strong and its footprints can be seen in Jupiter's polar regions. The interaction of Io with the plasma torus is in detail described by Kivelson et al. (2004) and Saur et al. (2004).

Let us describe the interaction briefly. At first we define coordinate system: the X-axis is oriented in the direction of the plasma flow, the Y-axis directs along the Jupiter's magnetic field $\mathbf{B}_J$ (i.e., southward) and the Z-axis, completing the right-handed system, directs to the Jupiter.

Drell et al. (1965) solved the linear set of Maxwell's equations to study the field perturbance caused by an ideally conducting object propagating through the plasma across the magnetic field. Such object feels a motional electric field which drives the electric current in the direction perpendicular to both magnetic field and direction of satellite motion. This current continues out of the satellite in the form of field aligned currents through the plasma. According to the analysis of Drell et al. (1965), the satellite generates low-frequency Alfvén disturbance which carries the current. Currents flow in the plane of satellite motion and magnetic field and aim to the back of satellite at angle α to the magnetic field such that

$$\tan\alpha = \frac{V_s}{V_A} = M_A.$$

Here V_s is the satellite velocity with respect to the plasma, V_A is Alfvén velocity of plasma and M_A is Alfvén Mach number. The structure of generated field aligned currents is called *Alfvén wing*.

This model is applicable to Io which is propagating through its plasma torus almost perpendicular to the Jovian magnetic field and can be considered to be conducting. It was discussed in the previous section that Io orbits with lower velocity than the torus and thus Io moves in the opposite direction in reference frame of the torus than in the reference frame of Jupiter. Consequently, generated Alfvén wings, which aim to the back of Io in the frame of torus, aim ahead of Io on its real trajectory.

In the unperturbed torus the flowing plasma generates electric field

$$\mathbf{E}_0 = -\mathbf{V}_{torus} \times \mathbf{B}_J.$$

in the reference frame of Io. This field is directed in the $-Z$-direction (i.e., away from Jupiter in the radial direction). Highly conducting dense ionosphere of Io can carry the current driven by this electric field in the direction

perpendicular to the magnetic field. Further from Io, where the perpendicular conductivity is negligible, currents can flow along the magnetic field only. In result, the interaction generates the circuit composed of magnetic field aligned current flowing towards Io on the Jupiter-facing side, ionospheric current flowing away from Jupiter in the radial direction, field aligned current flowing towards Jupiter on the anti-Jupiter side and closing current in Jovian ionosphere near the polar region. Total current flowing through Io is of the order of $10^5 - 10^6$ A according to Southwood et al. (1980) or Saur et al. (2002). Neubauer (1980) extended the linear theory of Drell et al. (1965) to the non-linear situation and applied it to the case of Io. He showed that the conductivity associated with Alfvén wings is

$$\Sigma_A = \frac{1}{\mu_0 V_A \left(1 + M_A^2 + 2M_A \sin\alpha\right)^{1/2}}$$

and the current circuit can close through the wings.

Alfvén waves can be reflected on the boundary of torus or in Jovian ionosphere. Since the wings aim ahead of Io on its trajectory, the reflected waves can reach Io and reflect again back to the Jupiter. It was proposed by Neubauer (1980) that this effect is partly responsible for the phenomenon known as *Io effect*, i.e., periodic fluctuations of radiation power from Jupiter which are correlated to Io's position.

The charge separation caused by the ionospheric current generates secondary electric field aiming in the direction towards Jupiter. This electric field acts to slow and divert the incoming torus flow. As a result, the frozen in magnetic field compresses upstream of Io.

2.4 Plasma waves at Io

The mass loading via ionization of neutrals can heat the flowing plasma and increase its temperature anisotropy $A = T_\perp/T_\parallel > 1$ (Linker et al. (1989)). Such anisotropy generates ion cyclotron and mirror waves which were both observed near Io.

Ion cyclotron waves have left-handed circular polarization, real frequencies below the ion cyclotron frequency and maximum growth rate for parallel propagation. Waves with SO_2^+, SO^+ and S^+ ion gyrofrequencies were detected during five flybys (namely I0, I24, I25, I31 and I32 where I refers to an Io flyby and the number is the orbit number) of *Galileo* around Io. Russell et al. (2003b) give the summary of these observations and show that the waves were rather elliptical polarized and propagated at slightly oblique angles with respect to the background magnetic field.

During the I0 flyby on December 7, 1995, *Galileo* flew in nearly radial direction to Jupiter in its equatorial plane and it passed Io at distance 1.5 R_{Io} in the wake. Cyclotron waves appeared at distance 18 R_{Io} on the inbound pass and disappeared at 7 R_{Io} on the outbound pass, but they were replaced by mirror waves on edges of Io's wake and linearly polarized transverse waves in the center of wake. Properties of cyclotron waves have been analyzed by Huddleston et al. (1997), Warnecke et al. (1997) or Russell et al. (1999b).

The dominant mode observed during I0 flyby was that of molecules of SO_2^+. The reason for this is in absence of thermalized SO_2^+ component in the background torus plasma; Huddleston et al. (1997) inferred that this component has density less than 5 % and Warnecke et al. (1997) estimated it to be below 2 %. The waves were detected with growing amplitude when *Galileo* approached closer to Io and with decreasing amplitude during the outbound pass. Moreover, the amplitude was higher on the inbound pass. The increase of amplitude with decreasing distance is consistent with the increase of ion production rate. Warnecke et al. (1997) have found that the wave power profile follows the neutral density profile on the inbound pass because there was constant electron density during the period of observations of cyclotron waves (according to the analysis of Gurnett et al. (1996)). Due to the constant electron density, the ion production rate due to electron impact ionization follows the neutral density profile. On the outbound pass, the electron density decreased radially from Io (Gurnett et al. (1996)) and consequently the ion production rate due to the electron impact ionization (and the wave power) fell off more rapidly than on the inbound pass.

There was also an asymmetry between the power spectra on the inbound and outbound passes; the power of SO^+-cyclotron waves increased on the outbound pass. The inbound pass of I0 flyby can be considered to be over the day hemisphere and the outbound pass can be considered to be over the night hemisphere. The asymmetry in the spectra can be attributed to the day-night asymmetry of the atmosphere composition.

I24 and I27 flybys had similar trajectories, *Galileo* crossed the axis of plasma flow in oblique direction and moved from upstream to downstream side. Cyclotron waves were observed on the downstream side mainly, but a small burst of waves was detected during the I24 pass upstream of Io right on the axis of plasma flow. The dominant mode was that of molecules of SO^+. Blanco-Cano et al. (2001) performed a dispersion analysis to study conditions for dominance of particular modes. They found that the SO^+-cyclotron mode exceeds the SO_2^+ mode when the density of SO^+ ions is at least twice higher than the density of SO_2^+.

The I31 pass in August 2001 was parallel to the flow in Io's northern hemisphere. *Galileo* passed Io parallel to the torus axis in the anti-Jovian

side and flew above the wake in the direction of plasma flow. Again, waves occurred downstream of Io and were probably excited in Io's wake (Russell et al. (2003a)). Trajectory of I32 flyby was similar to those of I24 and I27 passes but the measured spectra resembles rather that of I0 pass because the SO_2^+-cyclotron mode is dominant.

In conclusion, the cyclotron waves have been observed almost exclusively on Io's downstream side but the properties of waves differ from pass to pass. This fact implies variability of local plasma properties. Russell et al. (2003b) did not find any significant correlation between the wave properties and solar phase or position of *Galileo* with respect to Io and ascribed this variability to the variability of volcanic input at Io.

Mirror waves have linear polarization, zero real frequency and maximum growth rates at oblique angles to the ambient magnetic field. Mirror mode structures have large magnetic fluctuations which are anticorrelated with fluctuations in plasma density. Mirror waves were observed on both edges of Io's wake during *Galileo*'s first flyby in December 1995 (Russell et al. (1999a), Russell et al. (1999b)). The waves were nearly linearly polarized and propagated at angles about 80° to the ambient magnetic field.

The question which naturally arises is how the mirror mode can dominate in the very low-beta plasma at Io. The answer was given by Huddleston et al. (1999). They found that for the mirror mode to be dominant, in addition to large temperature anisotropy of SO_2^+ (the dominant species close to Io), high anisotropies of other torus species (namely S^+ and O^+) are necessary. In such cases the growth rate of the mirror mode exceeds the ion cyclotron mode growth rates for a particular ionic species. These conditions are filled on the edges of the wake where the densities of the torus S^+ and O^+ have decreased and thus this thermalized contribution can not sufficiently reduce the anisotropy of the pick-up particles.

Chapter 3

Model

Through the years many methods for numerical simulations of plasma were developed. Two basic approaches to the modelling are:

- kinetic models where both ions and electrons are modeled as separate particles
- and fluid models where ions and electrons are modeled as fluids.

Naturally both methods have advantages and disadvantages. Kinetic models are very time and memory consuming. For this reason the simulated areas and times are limited. Fluid models allow to model much larger plasmas for a longer time. On the other hand, fluid models can not resolve kinetic effects related to the Larmor radius.

The combination of mentioned models is the hybrid approach. Here the electrons are simulated as fluid while the ions as kinetic population. The electron fluid is massless and its role is to maintain the quasineutrality of plasma. Hybrid modelling enables to simulate more ions than kinetic because it does not require computer memory for electrons. Moreover, hybrid models can resolve ion kinetic effects in contrast to fluid models.

3.1 CAM-CL algorithm

One of hybrid models is *current advance method and cyclic leapfrog algorithm* (CAM-CL) developed by Matthews (1994). In this algorithm algorithm, the plasma is described by following set of equations:

- Faraday's law

$$\nabla \times \mathbf{E} = -\frac{\partial \mathbf{B}}{\partial t}, \tag{3.1}$$

- Ohm's law in the magnetostatic approximation

$$\mathbf{E} = \frac{1}{\rho_{c,\mathrm{i}}}\left(\frac{(\nabla\times\mathbf{B})\times\mathbf{B}}{\mu_0} - \mathbf{J}_\mathrm{i}\times\mathbf{B} - \nabla p_\mathrm{e}\right) + \eta\left(\nabla\times\mathbf{B}\right), \tag{3.2}$$

- Newton's law

$$\frac{d\mathbf{v}_s}{dt} = \frac{q_s}{m_s}\left(\mathbf{E} + \mathbf{v}_s\times\mathbf{B}\right), \tag{3.3}$$

- equation for ion position

$$\frac{d\mathbf{x}_s}{dt} = \mathbf{v}_s. \tag{3.4}$$

In relations (3.1) - (3.4), used quantities are electric field $\mathbf{E}$, magnetic field $\mathbf{B}$, ionic charge density $\rho_{c,\mathrm{i}}$, total ionic current density $\mathbf{J}_\mathrm{i} = \sum_s \mathbf{J}_s$ composed of current densities of particular ionic species $\mathbf{J}_s$, electron pressure $p_\mathrm{e} = n_\mathrm{e}k_B T_\mathrm{e}$, resistive term η and charge q_s, mass m_s, position $\mathbf{x}_s$ and velocity $\mathbf{v}_s$ of ions of species s. For purpose of CAM-CL this set is completed with the equation for time evolution of ionic current density which can be derived from the Newton's law (3.3)

$$\frac{d\mathbf{J}_\mathrm{i}}{dt} = \sum_s \frac{q_s}{m_s}\left(\rho_{c,s}\mathbf{E} + \mathbf{J}_s\times\mathbf{B}\right). \tag{3.5}$$

Let us describe here the algorithm for pushing particles from positions $\mathbf{x}\left(t_0 + \frac{1}{2}\Delta t\right)$ to positions $\mathbf{x}\left(t_0 + \frac{3}{2}\Delta t\right)$. We will use notation $g\left(t_0 + n\Delta t\right) = g^n$ and quantities Λ and Γ defined by relations

$$\Lambda = \sum_s r_s \rho_{c,s}^{1/2}, \tag{3.6}$$

$$\Gamma = \sum_s r_s \mathbf{J}_s(\mathbf{x}_s^{1/2}, \mathbf{v}_s^0) \tag{3.7}$$

where $\rho_{c,s}$ is the charge density and $r_s = q_s/m_s$ is the charge to mass ratio of the ionic species s. We omit the subindex s and we assume that, besides $\mathbf{x}^{1/2}$, following quantities are known at the beginning of each time step: $\mathbf{v}^0$, $\mathbf{B}^0$, ρ_c^0, $\rho_c^{1/2}$, $\mathbf{J}_\mathrm{i}^0$, Λ, Γ and $\mathbf{J}_\mathrm{i}(\mathbf{x}^{1/2}, \mathbf{v}^0)$.

Pushing of particles in kinetic simulations is done in two main steps, integration of Newton's law (3.3) and determination of new position from (3.4). The leapfrog method is used to push the particles in CAM-CL. Ion positions and velocities are computed in times half time step shifted so the new position can be determined from the central difference

$$\mathbf{x}^{3/2} = \mathbf{x}^{1/2} + \mathbf{v}^1\Delta t. \tag{3.8}$$

The required velocity $\mathbf{v}^1$ is computed from central difference applied on Newton's law with Lorentz force on the right side (3.3)

$$\mathbf{v}^1 = \mathbf{v}^0 + \Delta t \frac{q}{m} \left(\mathbf{E}^{1/2} + \mathbf{v}^{1/2} \times \mathbf{B}^{1/2} \right) \tag{3.9}$$

where $\mathbf{v}^{1/2}$ is computed from the relation

$$\mathbf{v}^{1/2} = \mathbf{v}^0 + \frac{\Delta t}{2} \frac{q}{m} \left(\mathbf{E}^{1/2} + \mathbf{v}^0 \times \mathbf{B}^{1/2} \right). \tag{3.10}$$

Determination of field quantities is the goal of *current advance method*. The procedure is done in following steps:

- The Faraday's law (3.1) is integrated to get $\mathbf{B}^{1/2}$

$$\mathbf{B}^{1/2} = \mathbf{B}^0 - \int_0^{\Delta t/2} \nabla \times \mathbf{E} \left(\rho_c^0, \mathbf{J}_\mathrm{i}^0, \mathbf{B}(t), T_e \right) dt.$$

  This step is done by *cyclic leapfrog* method discussed in next section.

- New electric field is computed from Ohm's law (3.2) using advanced $\mathbf{B}$ and ρ_c

$$\mathbf{E}^* = \mathbf{E} \left(\rho_{c,\mathrm{i}}^{1/2}, \mathbf{J}_\mathrm{i}(\mathbf{x}^{1/2}, \mathbf{v}^0), \mathbf{B}^{1/2}, T_\mathrm{e} \right).$$

- Ionic current density is advanced in velocity by integration of (3.5)

$$\mathbf{J}_\mathrm{i}^{1/2} = \mathbf{J}_\mathrm{i}(\mathbf{x}^{1/2}, \mathbf{v}^0) + \frac{\Delta t}{2} \left(\Lambda \mathbf{E}^* + \Gamma \times \mathbf{B}^{1/2} \right)$$

  where Λ and Γ are given by (3.6) and (3.7).

- Electric field is advanced to $\mathbf{E}^{1/2}$

$$\mathbf{E}^{1/2} = \mathbf{E} \left(\rho_{c,\mathrm{i}}^{1/2}, \mathbf{J}_\mathrm{i}^{1/2}, \mathbf{B}^{1/2}, T_\mathrm{e} \right).$$

Values of fields required for equations (3.9) and (3.10) are known so the particles can be pushed now by (3.8). In order to begin new time step a few quantities must be computed using new state $\mathbf{x}^{3/2}$ and $\mathbf{v}^1$:

$$\rho_{c,\mathrm{i}}^{3/2},$$

$$\rho_{c,\mathrm{i}}^{1} = \frac{1}{2}(\rho_{c,\mathrm{i}}^{1/2} + \rho_{c,\mathrm{i}}^{3/2}),$$

$$\mathbf{J}_{\mathrm{i}}(\mathbf{x}^{3/2}, \mathbf{v}^1),$$

$$\mathbf{J}_{\mathrm{i}}^1 = \frac{1}{2}\left(\mathbf{J}_{\mathrm{i}}(\mathbf{x}^{3/2}, \mathbf{v}^1) + \mathbf{J}_{\mathrm{i}}(\mathbf{x}^{1/2}, \mathbf{v}^1)\right),$$

$$\Lambda = \sum_s r_s \rho_{c,s}^{3/2}$$

and

$$\Gamma = \sum_s r_s \mathbf{J}_s(\mathbf{x}^{3/2}, \mathbf{v}^1).$$

Finally the magnetic field is advanced to $\mathbf{B}^1$ by the second use of cyclic leapfrog

$$\mathbf{B}^1 = \mathbf{B}^{1/2} - \int_{\Delta t/2}^{\Delta t} \nabla \times \mathbf{E}\left(\rho_{c,\mathrm{i}}^1, \mathbf{J}_{\mathrm{i}}^1, \mathbf{B}(t), T_{\mathrm{e}}\right) dt.$$

3.2 Implementation

In the previous section the CAM-CL algorithm was described just in general. In this section some details about implementation of the code are discussed.

Plasma in CAM-CL is modelled using the particle in cell scheme. The simulation domain is divided into $N_x \times N_y$ cells which form a rectangular grid. Moments $\rho_{c,\mathrm{i}}$, $\mathbf{J}_{\mathrm{i}}$, magnetic field $\mathbf{B}$ and electron pressure p_{e} are computed in nodes of this grid which will be called in the text *magnetic field grid*. The electric field has its own grid (*electric field grid*) whose nodes are located in centres of cells of the magnetic field grid, see Figure 3.1. Nodes of magnetic field grid are marked with full integer indices while the electric field grid nodes with half integer indices. We take particle positions to be also full integer in nodes of magnetic field grid.

3.2.1 Weighting

Every particle contributes to moments $\rho_{c,\mathrm{i}}$ and $\mathbf{J}_{\mathrm{i}}$ computed in corners of cell where the particle is located. Each particle has a weight equal to 1 and the contributions to the cell corners are determined from the particle position in the cell. The particle is located in the cell at position (x, y) as shown in figure 3.1 and it is a carrier of a quantity G. Contributions to cell corners are given as

$$G(i, j) = \phi_{dd}(x, y, i, j)G,$$

$$G(i+1, j) = \phi_{ud}(x, y, i+1, j)G,$$

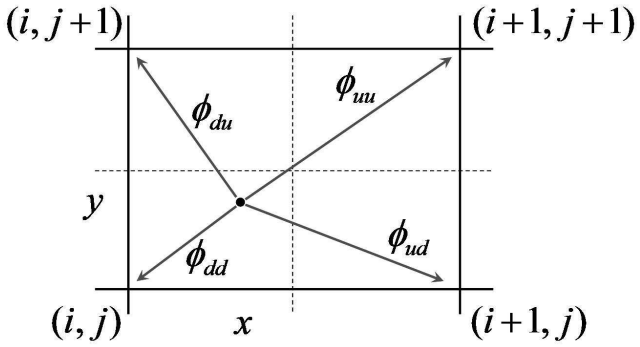

Figure 3.1: Sketch of the simulation cell: the full line grid is the *magnetic field grid* where moments $\rho_{c,\mathrm{i}}$, $\mathbf{J}_\mathrm{i}$ and magnetic field $\mathbf{B}$ are computed. Dashed lines represent *electric field grid*. Particle located at (x, y) contributes to moments computed in four nearest nodes of the magnetic field grid.

$$G(i, j+1) = \phi_{du}(x, y, i, j+1)G,$$
$$G(i+1, j+1) = \phi_{uu}(x, y, i+1, j+1)G$$

where the weights are

$$\phi_{dd}(x, y, i, j) = (1 - x + i)(1 - y + j),$$
$$\phi_{ud}(x, y, i+1, j) = (x - i)(1 - y + j),$$
$$\phi_{du}(x, y, i, j+1) = (1 - x + i)(y - j),$$
$$\phi_{uu}(x, y, i+1, j+1) = (x - i)(y - j).$$

Total value of G in some node is given by the sum of contributions of all particles located in neighbouring cells. For example determination of G in node (i, j) can be formally written

$$\begin{aligned} G(i,j) = \Phi(\mathbf{x}, i, j)G \;:=\; \sum_p [&\delta_{i\lceil x_p \rceil}\delta_{j\lceil y_p \rceil}\phi_{uu}(x_p, y_p, i, j)G_p + \\ &+\delta_{i\lfloor x_p \rfloor}\delta_{j\lceil y_p \rceil}\phi_{du}(x_p, y_p, i, j)G_p + \\ &+\delta_{i\lceil x_p \rceil}\delta_{j\lfloor y_p \rfloor}\phi_{ud}(x_p, y_p, i, j)G_p + \\ &+\delta_{i\lfloor x_p \rfloor}\delta_{j\lfloor y_p \rfloor}\phi_{dd}(x_p, y_p, i, j)G_p], \end{aligned}$$

where the summation is over all particles whose positions are stored in the vector $\mathbf{x}$, δ_{kl} is Kronecker delta, $\lceil\cdot\rceil$ and $\lfloor\cdot\rfloor$ are ceiling and floor functions, respectively.

3.2.2 Determination of moments

Using the weight operator Φ defined in the section 3.2.1 moments $\rho_{c,\mathrm{i}}$ and $\mathbf{J}_\mathrm{i}(\mathbf{x},\mathbf{v})$ in a node (i,j) can be computed from particle positions and velocities from relations

$$\rho_{c,\mathrm{i}}(i,j) = \sum_s \rho_{c,s}(i,j) = \sum_s \Phi(\mathbf{x}_s,i,j)q_s$$

and

$$\mathbf{J}_\mathrm{i}(\mathbf{x},\mathbf{v})(i,j) = \sum_s \mathbf{J}_s(i,j) = \sum_s \Phi(\mathbf{x}_s,i,j)q_s\mathbf{v}_s.$$

3.2.3 Electron pressure

The electron pressure is given by relation $p_\mathrm{e} = n_\mathrm{e}k_B T_\mathrm{e}$, where electron temperature T_e is in the hybrid code considered to be constant. We require plasma to be quasineutral so the concentration of electrons n_e can be computed from the total charge density

$$n_\mathrm{e} = \frac{\rho_{c,\mathrm{i}}}{e}.$$

3.2.4 Spatial derivatives

In CAM-CL derivatives transform some quantity from one grid to the second. For example, ∇p_e transform the pressure from the magnetic field grid to the electric field grid. The derivative in some node is computed from four nearest nodes of the second grid. Derivatives of g in the node $(i+\frac{1}{2},j+\frac{1}{2})$ in x and y directions are given by relations

$$\frac{\partial g}{\partial x}(i+\frac{1}{2},j+\frac{1}{2}) = \frac{1}{2\Delta x}\left(g(i+1,j+1)+g(i+1,j)-g(i,j+1)-g(i,j)\right),$$

$$\frac{\partial g}{\partial y}(i+\frac{1}{2},j+\frac{1}{2}) = \frac{1}{2\Delta y}\left(g(i+1,j+1)+g(i,j+1)-g(i+1,j)-g(i,j)\right).$$

Operators **rot** and **grad** used in CAM-CL can be simply computed using these relations.

3.2.5 Electric field

The value of electric field in the node $(i-\frac{1}{2},j-\frac{1}{2})$ is computed from Ohm's law (3.2). Here the values of $\nabla\times\mathbf{B}$ and ∇p_e are computed in the node $(i-\frac{1}{2},j-\frac{1}{2})$ using appropriate spatial derivatives and values of other quantities ($\mathbf{B}$, $\rho_{c,\mathrm{i}}$

and $\mathbf{J}_\mathrm{i}$) are given in the node $(i-\frac{1}{2}, j-\frac{1}{2})$ as average of values on four nearest nodes of magnetic field grid

$$\rho_c(i-\frac{1}{2}, j-\frac{1}{2}) = \frac{1}{4}\left(\rho_c(i-1,j-1) + \rho_c(i,j-1) + \rho_c(i-1,j) + \rho_c(i,j)\right).$$

The electric field (3.2) becomes divergent if the plasma vanishes in some region, for that reason the density is kept above some minimal value.

3.2.6 Magnetic field - Cyclic leapfrog algorithm

The integration of Faraday's law (3.1) in one single step could lead to significant simulation noise so the integration is done in few substeps. Let the magnetic field is to be advanced from $\mathbf{B}^0$ to $\mathbf{B}^{1/2}$

$$\mathbf{B}^{1/2} = \mathbf{B}^0 - \int_0^{\Delta t/2} \nabla \times \mathbf{E}\left(\rho_c^0, \mathbf{J}_\mathrm{i}^0, \mathbf{B}(t), T_\mathrm{e}\right) dt.$$

Magnetic field is advanced in n time substeps, each time substep is $\tau = \frac{\Delta t}{2n}$. The procedure is done in two ways, the magnetic field in odd times is leapfrogged by the field in even times and vice versa. This is the origin of name cyclic leapfrog. The scheme can be written as

$$\begin{aligned}
\mathbf{B}^{\tau} &= \mathbf{B}^0 - \tau\nabla\times\mathbf{E}\left(\rho_c^0, \mathbf{J}_\mathrm{i}^0, \mathbf{B}^0, T_\mathrm{e}\right),\\
\mathbf{B}^{2\tau} &= \mathbf{B}^0 - 2\tau\nabla\times\mathbf{E}\left(\rho_c^0, \mathbf{J}_\mathrm{i}^0, \mathbf{B}^{\tau}, T_\mathrm{e}\right),\\
\mathbf{B}^{3\tau} &= \mathbf{B}^{\tau} - 2\tau\nabla\times\mathbf{E}\left(\rho_c^0, \mathbf{J}_\mathrm{i}^0, \mathbf{B}^{2\tau}, T_\mathrm{e}\right),\\
&\vdots\\
\mathbf{B}^{(n-1)\tau} &= \mathbf{B}^{(n-3)\tau} - 2\tau\nabla\times\mathbf{E}\left(\rho_c^0, \mathbf{J}_\mathrm{i}^0, \mathbf{B}^{(n-2)\tau}, T_\mathrm{e}\right),\\
\mathbf{B}^{n\tau} &= \mathbf{B}^{(n-2)\tau} - 2\tau\nabla\times\mathbf{E}\left(\rho_c^0, \mathbf{J}_\mathrm{i}^0, \mathbf{B}^{(n-1)\tau}, T_\mathrm{e}\right),\\
\mathbf{B}_*^{n\tau} &= \mathbf{B}^{(n-1)\tau} - \tau\nabla\times\mathbf{E}\left(\rho_c^0, \mathbf{J}_\mathrm{i}^0, \mathbf{B}^{(n-1)\tau}, T_\mathrm{e}\right).
\end{aligned}$$

Finally we get $\mathbf{B}^{1/2}$

$$\mathbf{B}^{1/2} = \frac{1}{2}\left(\mathbf{B}^{n\tau} + \mathbf{B}_*^{n\tau}\right).$$

Typically about 5-10 substeps are used.

3.2.7 Boundary and initial conditions

Boundary conditions serve to terminate plasma parameters continuously on borders of the simulation domain. The discontinuity of quantities on borders would lead to development of artificial effects such as reflection of waves

or creation of artificial field. Two basic approaches are used to solve this problem: *periodic* and *open* boundary conditions. In the former approach particles which left the domain on one side are injected back on the opposite side with unchanged velocity. Values of moments in boundary nodes are added to moments on the opposite boundary. If the open boundary conditions are used, particles which left the domain are lost.

The simulation is scaled by values of background plasma parameters; values of ionic inertial length $\Lambda_{\mathrm{i}} = c/\omega_{p,\mathrm{i}}$, Alfvén velocity V_A and inversed ionic gyrofrequency $1/\omega_{g,\mathrm{i}}$ are taken as units of length, velocity and time. Ambient magnetic field B_0 and charge density $\rho_{c,0}$ are scaled to unity as well.

Direction of the background magnetic field, electron pressure and the background plasma properties are set as the initial condition. The plasma can contain more species and arbitrary parameters for each species are:

- relative density n_s and charge to mass ratio $r_s = q_s/m_s$ which define background plasma composition,
- parallel beta $\beta_{\parallel,s}$ and temperature anisotropy $A_s = T_{\perp,s}/T_{\parallel,s}$ which define pressures and temperatures of given species,
- direction and magnitude of the bulk velocity V_s (this determines the Alfvén Mach number $M_{A,s} = V_s/V_A$).

3.3 Previous models of Io-plasma torus interaction

The interaction of Io with its plasma torus has been studied intensively by means of numerical simulations. Most of the models were fluid. This section gives brief overview of the previous models.

Linker et al. (1989) used 3-D MHD model of the plasma flow past Io to examine the influence of the mass loading of plasma on its temperature. They included a source of the fresh plasma in the vicinity of Io with radially decreasing profile. They showed that the mass loading can increase the plasma temperature at Io.

Later, the same researchers (Linker et al. (1991)) used similar model without the source of the fresh plasma to study the interaction of magnetized plasma flow with conducting sphere representing Io and its thin ionosphere. The results include main global features of the interaction: formation of Alfvén wings and the diversion of the flow around wings and Io. Results indicate also the presence of slow and fast MHD modes.

More accurate models came after *Galileo*'s first flybys around Io. Linker et al. (1998) included both ionization and charge exchange processes in their 3-D MHD model and considered Io to be either conducting or intrinsically magnetized body. They obtained decreased magnetic field magnitude and increased plasma density in the wake as observed by *Galileo* but without the double peak structure in magnetic field on the flanks of wake. Better results were achieved with intrinsically magnetized Io.

Combi et al. (1998) obtained similar results in 3-D model without intrinsic magnetic field for Io. They used a cartesian grid with adaptive mesh. This model was lately slightly modified by Kabin et al. (2001) by changing the model of pick-up processes and introducing the day-night asymmetry in the distribution of the mass loading. The modified model provided better accordance of the simulation and observational data.

Saur et al. (1999) used 3-D two-fluid model for electrons and one plasma species. They assumed constant magnetic field in their model and included photoionization and electron impact ionization in the neutral atmosphere. They analyzed both numerically and analytically the effect of perpendicular Hall and Pedersen conductivities on the plasma flow. They showed that the flow is asymmetric around Io, the electrons are twisted toward Jupiter while the ions are diverted away.

The same group (Saur et al. (2002)) used modified model and obtained good agreement of the simulation and *Galileo* data including the double-peak structure in magnetic field in Io's wake. They explain this structure to be result of the diamagnetic and inertial currents which flow on the edges of wake. They used, besides photoionization and electron impact ionization, an additional ionization source of energetic field aligned beams of electrons (such beams were observed by Williams et al. (1999)).

Recently, Lipatov and Combi (2006) developed 3-D hybrid (kinetic ions and fluid electrons) model to study the effect of kinetic processes on the interaction. They implemented charge exchange, electron impact ionization and photoionization processes in a two-component neutral atmosphere with the radial profile

$$n_n(r) = n_{atm}\left[W_{int}\exp\left(-\frac{r-R_{Io}}{H_{atm}}\right) + W_{ext}\frac{H_{atm}}{4}\frac{R_{Io}}{r^2}\right] \tag{3.11}$$

where the first term represents a dense thin exosphere close to Io's surface while the second represents extended neutral clouds far from Io. In the equation (3.11), W_{int}, W_{ext} are fractions of the ion production rate in the exosphere and in the extended clouds, H_{atm} is the atmosphere scale height and n_{atm} is neutral density close to Io's surface. They were able to reproduce

observations of *Galileo* in Io's wake without using the beams of energetic electrons as in the simulation by Saur et al. (2002).

3.4 Details of used model

We can consider the plasma to be quasineutral on spatial scales of the space plasma. For this reason the hybrid code is very suitable for simulations of space plasmas. CAM-CL algorithm has been used successfully for simulations of plasma interactions with various space obstacles, such as Mercury (Trávníček et al. (2007)) or Moon (Trávníček et al. (2005)).

Each space obstacle has its specific features which must be included in the simulation properly. For example, the planet can have its magnetosphere or ionosphere, it can be magnetized or conducting etc.

Io is considered to be conducting and does not have significant magnetic field. The conductivity is provided by the function which sets the electric field inside Io to zero every time it is computed from Ohm's law (3.2).

Important feature of Io is presence of neutral atmosphere which is source of fresh plasma through ionization processes, such as electron impact ionization and photoionization. Moreover, the atmosphere is a target for incoming torus plasma ions which exchange charge with atmospheric neutrals. We include these ionization processes to the simulation. We treat separately charge exchange ionization and photoionization/electron impact ionization.

3.4.1 Charge exchange ionization

We use the model of charge exchange ionization proposed by Lipatov et al. (1998). Let us consider plasma species with velocity distribution function $f_p(\mathbf{v}_p)$ and neutral component with distribution function $f_n(\mathbf{v}_n)$. The loss rate for plasma, i.e., the time change of plasma velocity distribution function due to the charge exchange collisions with neutrals, is given by Ripken and Fahr (1983) as

$$\frac{\partial f_p(\mathbf{v}_p)}{\partial t} = f_p(\mathbf{v}_p) \cdot \int f_n(\mathbf{v}_n) v_{rel} \sigma_{ex}(v_{rel}) d^3\mathbf{v}_n. \tag{3.12}$$

In the integral, $v_{rel} = |\mathbf{v}_p - \mathbf{v}_n|$ is relative velocity between the plasma ion with velocity $\mathbf{v}_p$ and the neutral particle with velocity $\mathbf{v}_n$ and $\sigma_{ex}(v_{rel})$ is cross-section of charge exchange. If we assume cross-section independent on the relative velocity, the loss rate (3.12) becomes

$$\frac{\partial f_p(\mathbf{v}_p)}{\partial t} = f_p(\mathbf{v}_p) \cdot n_n \left|\mathbf{v}_p - \langle \mathbf{v}_n \rangle\right| \sigma_{ex} = f_p(\mathbf{v}_p) \cdot \beta_{ex}(\mathbf{v}_p) \tag{3.13}$$

where n_n is density of neutrals and $\langle \mathbf{v}_n \rangle$ is mean velocity of neutrals. Term $\beta_{ex}(\mathbf{v}_p) = n_n \left| \mathbf{v}_p - \langle \mathbf{v}_n \rangle \right| \sigma_{ex}$ has meaning of charge exchange rate for ions with velocity $\mathbf{v}_p$.

The probability that ion does not undergo the charge exchange during time interval $\Delta t = (t_0, t)$ is

$$p_{ex} = \exp\left[- \int_{t_0}^{t} \beta_{ex}(\mathbf{v}_p) dt \right]. \tag{3.14}$$

Naturally, the probability decreases with the length of the time interval and charge exchange rate $\beta_{ex}(\mathbf{v}_p)$. For time interval equal to the inversed charge exchange rate $\Delta t = \beta_{ex}^{-1}(\mathbf{v}_p)$, the survival probability is small which is required feature.

Escape velocity of neutrals at Io is estimated to be about (2.3-2.5) km.s^{-1} (Linker et al. (1985)). Since the torus bulk velocity relative to Io is $V_{rel} = 57$ km.s^{-1}, neutrals can be considered to be at rest with respect to the torus plasma and $\langle \mathbf{v}_n \rangle = 0$ in relation (3.13). If the time interval Δt is so small that charge exchange rate does not change significantly along the particle trajectory, the survival probability (3.14) is

$$p_{ex} = \exp\left[-\beta_{ex}(\mathbf{v}_p) \Delta t \right] = \exp\left[-n_n \left| \mathbf{v}_p \right| \sigma_{ex} \Delta t \right]. \tag{3.15}$$

We examine the survival probability (3.15) for each particle and compare it to the random number $\xi \in (0, 1)$. We exchange charge of those particles which fulfil relation $p_{ex} \leq \xi$. Since we assume the new ions created in Io's vicinity to be of the same species as the torus ions, the charge exchange is done simply by setting the ion velocity to zero.

3.4.2 Electron impact and photoionization

We inject ions created in photoionization together with those created in electron impact ionization. In other words we consider only total source rate of these processes. Each timestep we inject new ions within the vicinity of Io with required radial profile. The number of ions to be created in one time step is inferred from the total ion production rate at Io.

We require ion production rate density profile $q(r) = k \cdot f(r)$ within the sphere of radius R_{max} and we know the total ion production rate (number of neutral particles ionized per second) in this sphere Q_{ion}. In two dimensional simulation, we inject particles to the hollow cylinder with outer radius R_{max} and height dz, the ion production rate Q in this hollow cylinder is given as

$$Q = 2\pi k \cdot dz \cdot \int_{R_{Io}}^{R_{max}} f(r) \cdot r \cdot dr, \tag{3.16}$$

where the normalization constant k is computed from

$$Q_{ion} = 4\pi k \cdot \int_{R_{Io}}^{R_{max}} f(r) \cdot r^2 \cdot dr. \tag{3.17}$$

Q indicates number of real ions to be produced per one second in the hollow cylinder around Io. This number has to be recalculated to get the number of macroparticles to be produced per one timestep.

We inject each new ion with coordinates $x = r_p \cdot \sin(\varphi)$ and $y = r_p \cdot \cos(\varphi)$ relative to Io, Io's center is origin of the coordinate system. Polar angle φ is random with uniform distribution between 0 and 2π. Radial distance r_p is random too, but such that the density of newly created ions have radial profile $q(r)$. To obtain this profile the distance r_p is generated by following procedure:

- Random distance r_p between R_{Io} and R_{max} is generated.
- Ion production rate density is evaluated at this distance to get $q(r_p)$.
- Random number q_{random} between 0 and q_{max} is generated. Here q_{max} is maximal value of $q(r)$ on the interval (R_{Io},R_{max}), for decreasing profiles it is $q_{max} = q(r = R_{Io})$.
- If $q_{random} < q(r_p)$, the particle is injected to distance r_p, otherwise whole procedure is repeated.

The generation of distance can be simplified in some special cases. For example, if the ion production rate profile density is $q(r) \propto r^{-1}$, the distance from Io can be computed as $r_p = R_{max}^{\alpha} \cdot R_{Io}^{1-\alpha}$ where α is random number with uniform distribution between 0 and 1.

We assume atmospheric neutrals to be in rest with respect to Io so the new ions are created with zero bulk and thermal velocities. Subsequently, the contribution of each new ion is added to the charge density.

Chapter 4

Results

We will show results of hybrid simulations of plasma torus interaction with Io in this section. The simulations differ from each other in properties of Io's atmosphere/ionosphere. We study the interaction of Io with its plasma torus in dependence on two main parameters: ion production rate in the vicinity of Io Q_{ion} and surface neutral density n_{atm} which determines the rate of charge exchanges between plasma ions and atmosphere neutrals.

4.1 Simulation setup and overview

We will give brief overview of performed simulations at first. All the simulations are two dimensional in the plane $X - Y$ (see section 2.3). The X-axis directs along the plasma torus flow direction and the Y-axis directs along the Jovian background magnetic field $\mathbf{B}_J$. Whole simulation domain is filled with torus plasma and homogenous background magnetic field at the beginning of the simulation. New ions are continually injected to the simulation during the run. New ions are injected in the vicinity of Io within a sphere of radius $R_{max} = 5.6R_{Io}$

Overview of performed simulations is given in Table 4.1. Simulations differ in properties of the neutral atmosphere. The ion production rate is of the order of 10^{27} s^{-1}, three values have been used in simulations: $Q_{ion} = 0.5; 5; 20 \cdot 10^{27}$ s^{-1}. The surface neutral density n_{atm} scales the neutral density profile (4.1) of Lipatov and Combi (2006)

$$n_n(r) = n_{atm} \left[W_{int} \exp\left(-\frac{r - R_{Io}}{H_{atm}} \right) + W_{ext} \frac{H_{atm}}{4} \frac{R_{Io}}{r^2} \right] \qquad (4.1)$$

and determines the rate of charge exchanges between ions and neutrals (see section 3.4.1). In the profile (4.1) W_{int}, W_{ext} are fractions of the neutral

Run	Q_{ion}	n_{atm}
rm1-q5-sd05	5	0.5
rm1-q5-sd10	5	10
rm1-q05-sd05	0.5	0.5
rm1-q05-sd10	0.5	10
rm1-q20-sd05	20	0.5
rm1-q20-sd10	20	10
rm1-q5-nocx	5	-
lip-q20-sd05	20	0.5
lip-q20-sd10	20	10

Table 4.1: List of performed simulations. Values of ion production rate Q_{ion} due to the photoionization and electron impact ionization are given in 10^{27} s^{-1}. Values of surface neutral density n_{atm} are given in 10^8 cm^{-3}. Simulations with *rm1* in the name of the run have radial profile of ion production rate given as $q(r) \propto r^{-1}$ and the neutral atmosphere profile for charge exchange given as 4.1 according to Lipatov and Combi (2006). We use atmosphere scale height $H_{atm} = 0.5R_{Io}$. Simulations with *lip* in the name of the run have both the radial profile of newly injected ions and the neutral atmosphere profile for charge exchange given as n_n from (4.1) according to Lipatov and Combi (2006). In this case we use atmosphere scale height $H_{atm} = 0.1R_{Io}$.

atmosphere components ($W_{int} + W_{ext} = 1$), H_{atm} is atmosphere scale height. Lipatov and Combi (2006) used values of surface neutral density $n_{atm} \in (0.5 - 10) \cdot 10^8$ cm^{-3}, we use the extreme values in our simulations. We have performed also a simulation without the charge exchange.

We use two spatial profiles of ions created in electron impact and photoionization processes (see section 3.4.2). The first profile is $q(r) \propto r^{-1}$, in this case we use profile for charge exchange ionization n_n from (4.1) with $W_{int} = W_{ext} = 0.5$ and $H_{atm} = 0.5R_{Io}$. The second profile is $q(r) \propto n_n(r)$ with $W_{int} = W_{ext} = 0.5$ and $H_{atm} = 0.1R_{Io}$.

The initial torus plasma is composed of isotropic electrons and isotropic Maxwellian ions with mass $m_\mathrm{i} = 22m_\mathrm{p}$ and charge $q_\mathrm{i} = -q_\mathrm{e}$. These particles represent mean ions in the plasma torus with composition similar to that of the *Voyager 1* era (see Table 2.1). The unperturbed torus plasma has density $n_0 = 3500$ cm^{-3} and flows along the X-axis with velocity $V_0 = 0.3V_A$. We use torus pressure such that $\beta_{\mathrm{i},0} = 0.06$ and $\beta_\mathrm{e} = 0.0022$. While the value of electron beta is real, the value of ionic beta is approximately twice higher than the maximum value in table 2.2.

The simulation is scaled by properties of unperturbed torus plasma. Units

of time and length are inversed cyclotron frequency $1/\omega_{c,0}$ and ionic inertial length $\Lambda_0 = c/\omega_{p,0}$ where $\omega_{p,0}$ is plasma frequency in the unperturbed torus. Standard spatial resolution is $\Delta x = \Delta y = 0.2\Lambda_0$ and temporal resolution is $\Delta t = 0.02/\omega_{c,0}$. Typical gyroradius of the ions with $\beta_{\mathrm{i},0} = 0.06$ is $r_L = 2\sqrt{\beta_{\mathrm{i},0}/\pi}\Lambda_0 = 0.28\Lambda_0$ so the used cell size should be sufficient to resolve the gyroradius effects. A simulation with better resolution $\Delta x = \Delta y = 0.1\Lambda_0$ and $\Delta t = 0.01/\omega_{c,0}$ has been performed to check whether results are influenced by the cell size.

Ionic inertial length in plasma having above defined properties is $\Lambda_0 = 18$ km which is approximately hundred times smaller than the real Io radius $R_{Io} = 1821$ km. It follows that it is impossible to model the interaction on real scales. We use the Io radius $R_{Io,sim}$ scaled down with respect to real radius by $R_{Io}/R_{Io,sim} \approx 10$ so that the simulation radius is $R_{Io,sim} = 10\Lambda_0$. This radius is still much larger than the typical gyroradius $r_L = 0.28\Lambda_0$. The simulation domain has 1600 cells in both directions so the total size of the domain is $L_x = L_y = 32R_{Io}$. Total simulation time is $T = 500/\omega_{c,0}$.

We use periodic boundary conditions at borders of the simulation domain. The electric field and bulk velocity are set to zero in the interior of Io and particles hitting Io's surface are removed from the simulation.

Simulations were computed using the MPI protocol on 64 or 128 parallel nodes of the *Amalka Supercomputing Facility* at the Academy of Sciences of the Czech Republic. The simulation domain is divided into required number of equally sized subdomains and each node computes the code in one subdomain.

4.2 Global behaviour

Let us start with the description of the global behaviour of the interaction. Figure 4.1 shows the density of torus and pick-up plasma around Io at time $t = 500/\omega_{c,\mathrm{i}}$ from simulation *rm1-q5-sd05* with total ionization rate due to electron impact and photoionization $Q_{ion} = 5 \cdot 10^{27}$ s^{-1} and surface neutral density $n_{atm} = 0.5 \cdot 10^8$ cm^{-3}.

Pick-up ions form a denser cloud than the torus plasma and torus ions in the result accumulate on the upstream side of the ionosphere. pick-up ions are situated around Io in the sphere of radius $R_{max} = 5.6R_{Io}$ mainly and leave this region on the downstream side. The density of pick-up plasma is increased in the wake. Strongest fluctuations are present upstream of Io.

As torus ions reach the ionosphere, they are slowed down and deflected from the direction of initial flow (i.e., along the X-axis). Figure 4.2 shows the velocity of torus and pick-up ions in $X-Y$ plane. The color-scale plot repre-

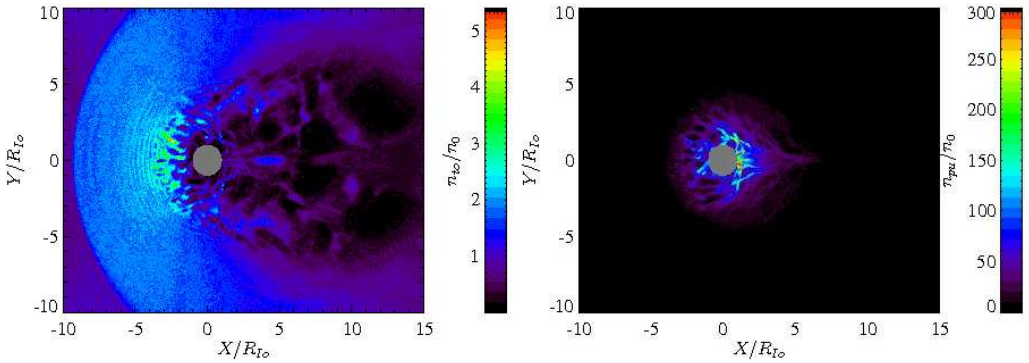

Figure 4.1: Distribution of plasma density around Io at time $T = 500/\omega_{c,0}$ from simulation *rm1-q5-sd05* with ion production rate $Q_{ion} = 5 \cdot 10^{27}$ s^{-1} and surface neutral density $n_{atm} = 0.5 \cdot 10^8$ cm^{-3}. The pick-up plasma (right) form dense ionosphere around Io. Torus ions (left) slow down in the region upstream of Io due to the presence of dense pick-up ionosphere and accumulate here.

sents the magnitude of the mean velocity in that plane $U_{xy,s} = \sqrt{U_{x,s}^2 + U_{y,s}^2}$. White arrows show the weighted direction of flow in given location. Each arrow represents the direction weighted from neighbouring cells using the bilinear weight. Pick-up plasma is dragged by the torus plasma away from Io in the direction of the torus flow. It can be seen that both components can locally (on the upstream side) flow away from Io in the direction opposite to the initial torus flow.

Figure 4.3 shows the simulated magnetic field from the same simulation *rm1-q5-sd05* as in previous Figures 4.1 and 4.2. Top panel displays the field in the $X - Y$ plane and the color and arrows have same meaning as in the Figure 4.2 of torus plasma flow. Color represents a magnitude of magnetic field in the plane and arrows represent the direction. The accumulation of plasma particles upstream of Io causes a compression of the magnetic field. When the torus plasma reaches the ionosphere, the initial magnetic field in the Y-direction is twisted around Io. The magnetic field is decreased downstream of Io; strong drop-off is present in the wake of Io where the magnetic field magnitude falls almost to zero. On the contrary, the density of plasma is increased in the wake. Bottom panel displays the z-component of the magnetic field. Strong fluctuations of the magnetic field are present mainly in close vicinity of Io.

We have performed a test simulation with the same parameters as in the simulation *rm1-q5-sd05* with better resolution in space and time to check

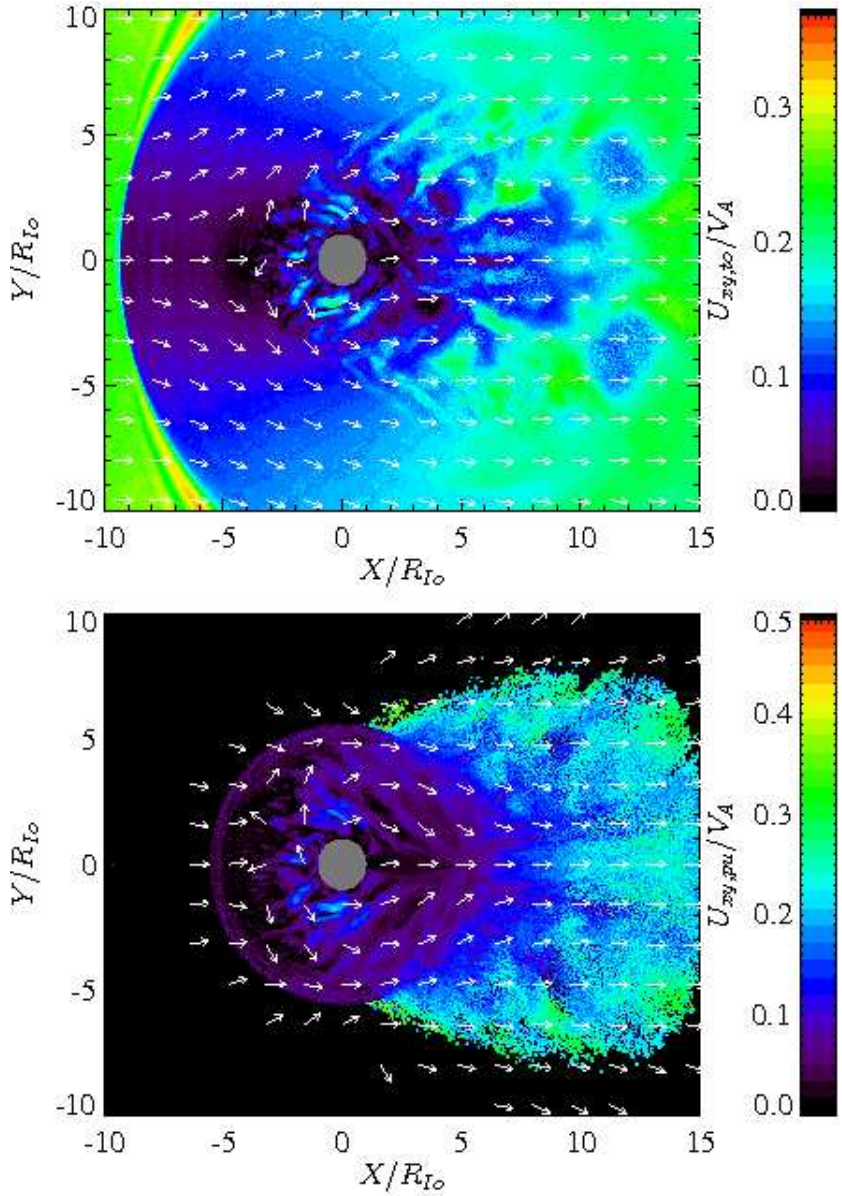

Figure 4.2: Velocity of the plasma in $X - Y$ plane from simulation *rm1-q5-sd05*. Color represents the magnitude of velocity and arrows represent the direction. Torus ions (top), which flow to Io with velocity $0.3V_A$, are slowed down upstream of Io and deflected around it. Downstream of Io, torus ions flow in the initial direction with lowered velocity. Pick-up ions (bottom) are dragged by the torus plasma and gain the velocity component in the X-direction.

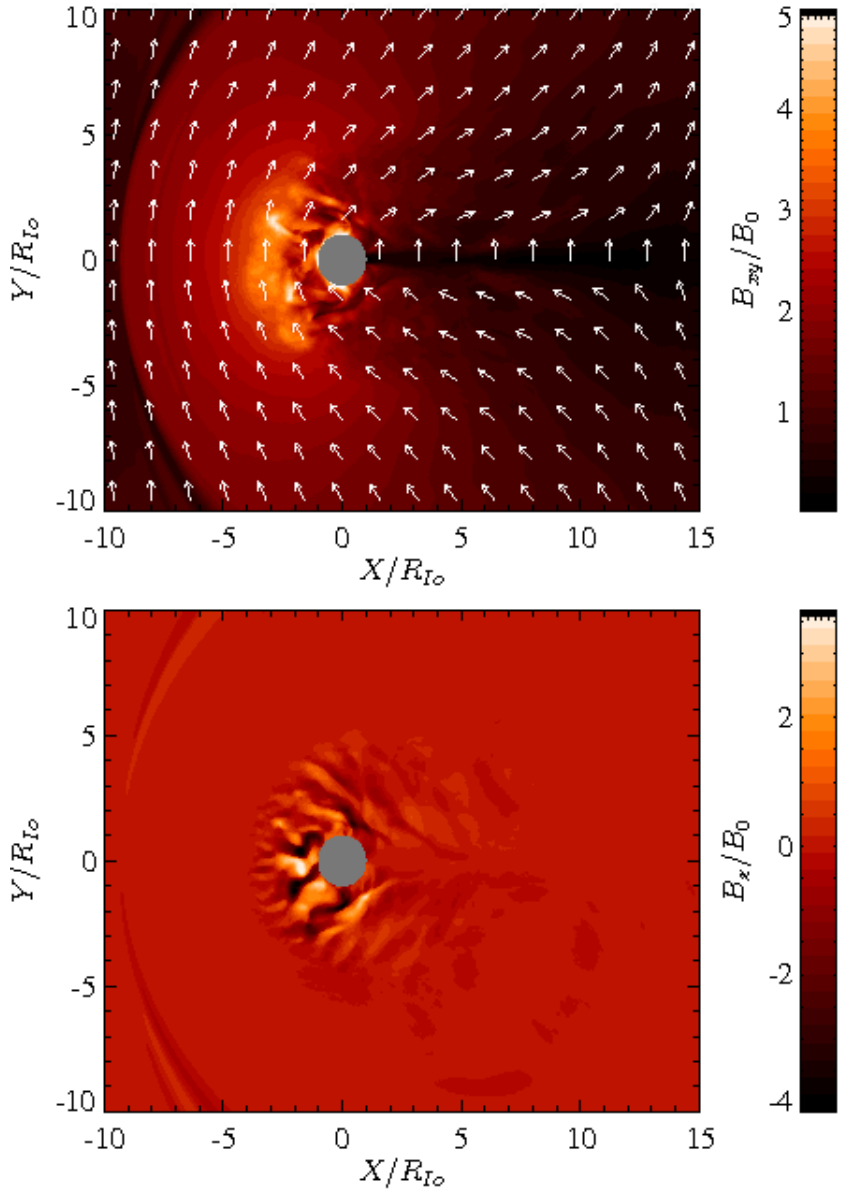

Figure 4.3: Magnetic field from simulation *rm1-q5-sd05*. Top panel shows the magnitude and direction of the field in $X-Y$ plane. The field is compressed upstream of Io and twisted around. In the wake, the field is decreased. Bottom panel shows the z-component of the magnetic field. Strong fluctuations can be seen close to Io in both panels.

whether results are affected by the cell size. We used resolution $\Delta x = \Delta y = 0.1\Lambda_0$ and $\Delta t = 0.01/\omega_{c,0}$. We have also performed a test simulation with higher number of particles per cell. Both test simulations give qualitatively same results as the simulation *rm1-q5-sd05*.

Naturally, all performed simulations manifest similar global behaviour as the discussed simulation *rm1-q5-sd05*: the field is compressed upstream of Io and is decreased downstream, plasma density is increased in the wake etc. Simulations differ mainly in the density of the ionosphere (which depends on the value of Q_{ion}) and the level of fluctuations close to Io. Simulations with low ionization rate $Q_{ion} = 0.5 \cdot 10^{27}$ have low density of pick-up ions and the fluctuations are weak. On the other hand, the ability of the torus plasma to drag ions from the ionosphere is lower for higher Q_{ion}. The surface neutral density n_{atm} determines the rate of charge exchanges and affects mainly the level of fluctuations which is generally lower for simulations with high n_{atm}.

For comparison, we show plots of densities from simulation *rm1-q5-sd10* with the same ion production rate Q_{ion} and higher surface neutral density n_{atm}. Resulting distribution of density is affected mainly in the close proximity to Io where ions exchange charge with neutrals most frequently. Since only one plasma species is used and newly created particles begin their life with zero velocity, exchanging the charge of ion with neutral is equivalent to stopping the ion. The plasma near Io is standing due to the high charge exchange rate; there are no fluctuations in comparison with simulation with low charge exchange rate. It would be seen in the figure of velocity similar to the Figure 4.2 that in the region around Io the velocity is close to zero.

4.3 Fluctuations

We will discuss the presence and properties of fluctuations close to Io in particular simulations. We examine the evolution of temperature anisotropy and the level of fluctuations at Io.

To study properties of fluctuations we compute the correlation coefficient between fluctuations of magnetic field and plasma density. We use the Pearson's correlation coefficient defined by the relation

$$\langle n_s, B \rangle = \frac{\sum_k \left(n_{s,k} - \overline{n_s}\right)\left(B_k - \overline{B}\right)}{(K-1)\,\sigma_{n_s}\sigma_B} \tag{4.2}$$

where σ is standard deviation of density or magnetic field and the overline denotes mean value on the sample, K is number of cells used for the computation. We use samples of 25×25 cells around the given point.

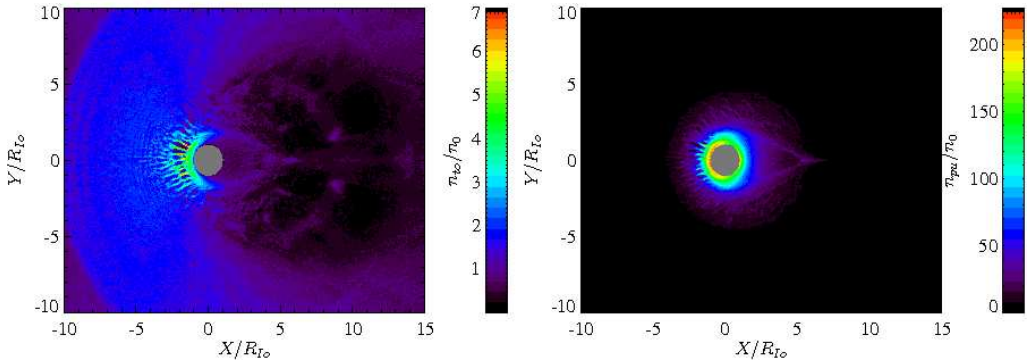

Figure 4.4: Density of torus plasma from simulation *rm1-q5-sd10* with same ionization rate Q_{ion} but higher surface neutral density n_{atm} than in the simulation from Figure 4.1. The charge exchange rate is high close to Io and the plasma here is almost immobile. Higher charge exchange rate decreases significantly the level of fluctuations in the plasma.

We look also on the distribution of the plasma in the $\beta_{\parallel,s} - A_s$ space. It has been discussed in chapter 1 that temperature anisotropy driven instabilities act to decrease the distance of plasma from isotropy, i.e., the quantity $|A_s - 1|$. Thus the instabilities constrain the dependence of maximum anisotropy on parallel beta to the shape which is related to the dependence of the instability growth rate on plasma parameters. The shape of constraints of the temperature anisotropy in the $\beta_{\parallel,s} - A_s$ space can be considered as an indirect indicator of the instability growth. We compute histograms of temperature anisotropy and parallel beta of the simulated plasma to compare the position of the plasma in the $\beta_{\parallel,s} - A_s$ with isocontours of the maximum growth rate of the anisotropy driven instabilities from Figure 1.1.

Basic simulation: $Q_{ion} = 5 \cdot 10^{27}$ s^{-1}; $n_{atm} = 0.5 \cdot 10^{8}$ cm^{-3}

We show simulated temperature anisotropy $A_s = T_{\perp,s}/T_{\parallel,s}$ from the simulation *rm1-q5-sd05* for torus ions and pick-up ions in Figure 4.5. The anisotropy is computed as the fraction of perpendicular and parallel pressures in the cells with sufficient number of macroparticles. The anisotropy is set to $A_s = 1$ in cells with less than five macroparticles.

The newborn pick-up ions have typically ring-type distribution function with large temperature anisotropy $A_{pu} > 1$ and low parallel beta at the beginning of their life. Such anisotropy may drive ion cyclotron and mirror instabilities which act to decrease the anisotropy. It has been showed in the

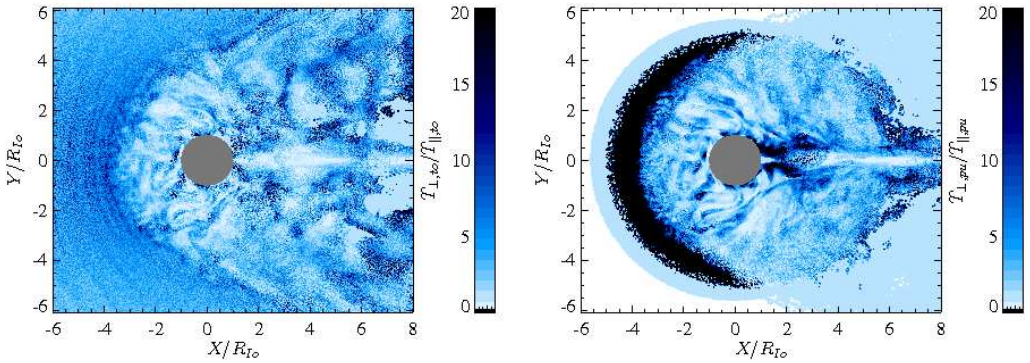

Figure 4.5: Temperature anisotropies of torus ions (left) and pick-up ions (right) from simulation *rm1-q5-sd05*. The temperature anisotropy has moderate values $A_s \lesssim 5$ in the region of high level of fluctuations (see Figures 4.1 and 4.3) probably due to the growth of temperature anisotropy driven instabilities.

figures of magnetic field and densities from the same simulation, i.e., in the Figures 4.3 and 4.1, that the fluctuations grew to the high levels close to Io.

There is a region of high anisotropy of pick-up plasma $A_{pu} \geq 20$ upstream of Io even though the number of macroparticles here is high. There are no fluctuations of density and field in this region. There probably exists some effect which does not allow the anisotropy driven instabilities to grow and reduce the anisotropy in this region. The reason could be for example in the fraction of densities of thermalized torus plasma and new pick-up plasma. Anisotropy driven instabilities are strongly damped in the plasma with low fraction of anisotropic contribution. However, the fraction of densities in the region in question is $n_{pu}/n_{to} \leq 5$ and the torus plasma is also anisotropic in the region probably due to the compression of magnetic field and thus this explanation does not seem to be valid. More likely, the high anisotropy is caused by the numerical effect. The compression of the magnetic field upstream of Io can cause that the Larmor radius drops below the resolution of the code.

The correlation coefficients (4.2) between fluctuations of density and magnetic field are showed in the Figure 4.6 for both plasma components. Strong anticorrelation between the fluctuations can be seen in the vicinity of Io on the upstream side. The orange region of high correlation between oscillations of density and magnetic field is related to the region of high anisotropy in Figure 4.5. There are no fluctuations so the density of pick-up plasma, which is increasing radially towards Io, is correlated with compressing magnetic field.

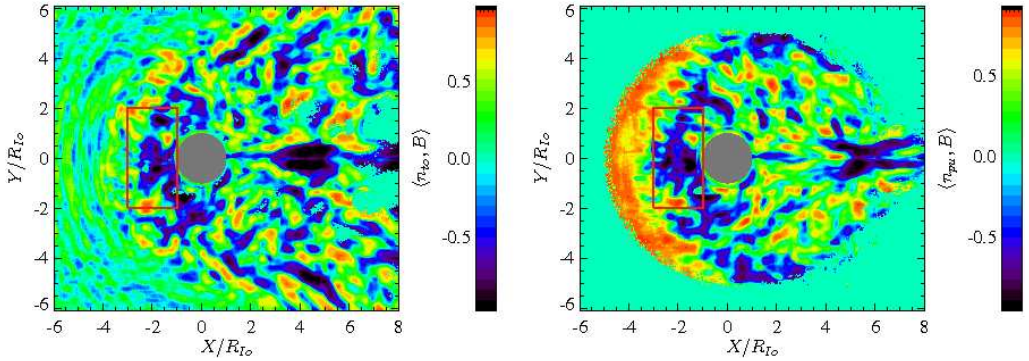

Figure 4.6: Correlation coefficient between the fluctuations of plasma density and magnetic field from the simulation *rm1-q5-sd05*. Left panel shows the correlation coefficient for fluctuations of the density of torus plasma and right panel represents the correlation coefficient for fluctuations of the density of pick-up plasma. Strong anticorrelation between fluctuations of density and magnetic field can be seen upstream of Io in the region of high fluctuations (marked roughly by the red box).

The anticorrelation between the fluctuations of magnetic field and plasma density on the downstream side in Figure 4.6 is a result of the interaction. Ions flow towards the axis of the domain on the downstream side (according to the Figure 4.2) and thus form region of increased density on the axis while the magnetic field is decreased on the axis.

Figure 4.7 shows the histogram of parallel beta $\beta_{\parallel,s}$ versus temperature anisotropy A_s for cells from the red box in Figure 4.6. The color represents normalized number of cells with given parallel beta and anisotropy. The figure contains isocontours of the maximum growth rate of ion cyclotron (solid), mirror (dashed) and parallel fire hose (dotted) instabilities. These isocontours are computed from linear Vlasov theory for plasma composed of isotropic electrons and bi-Maxwellian ions. Numbers on the lines denote the value of growth rate in unit of cyclotron frequency.

The incoming torus plasma is isotropic with $\beta_{\parallel,to} = 0.06$. In the red region, the torus plasma is shifted to higher anisotropies and lower parallel beta and lies below the threshold of ion cyclotron instability. The pick-up plasma has larger parallel beta than the torus plasma due to the higher density. The pick-up plasma lies in the unstable region and is constrained well with the isocontour $\gamma = 0.001\omega_c$ of the mirror instability.

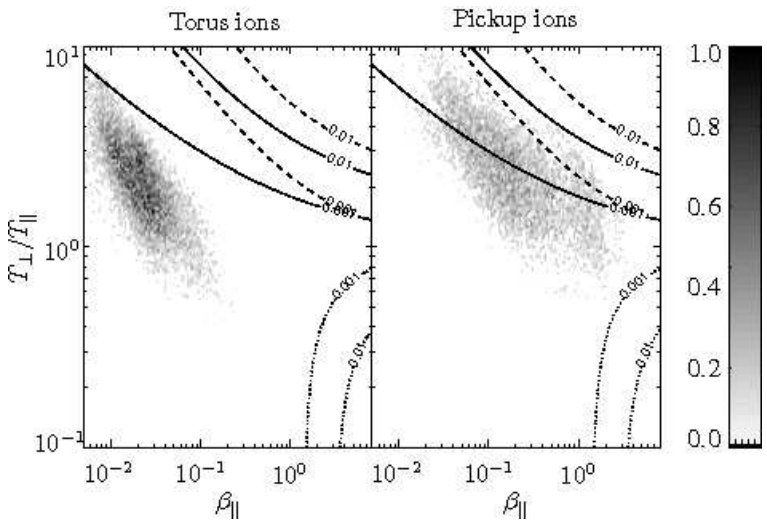

Figure 4.7: Histogram of the parallel beta versus temperature anisotropy from the simulation *rm1-q5-sd05* for the cells from red box in Figure 4.6. The pick-up plasma anisotropy is constrained quite well with the maximum growth rate $\gamma = 0.001\omega_c$ of the mirror instability.

Higher charge exchange rate: $Q_{ion} = 5 \cdot 10^{27}$ s^{-1}; $n_{atm} = 10 \cdot 10^{8}$ cm^{-3}

We show the correlation coefficient (4.2) between oscillations of plasma density and magnetic field from the simulation *rm1-q5-sd10* with higher surface neutral density than in the simulation *rm1-q5-sd05* in Figure 4.8. It has been showed in the Figure 4.4 that the higher surface neutral density causes that there is much lower level of fluctuations totally and no fluctuations very close to Io. It follows that the correlation coefficient is significantly changed as well. The anticorrelation of fluctuations observed in the simulation with low charge exchange rate in Figure 4.6 almost vanished in this simulation.

We show the histogram of parallel beta versus temperature anisotropy from this simulation in Figure 4.9. The box is the same as in the Figure 4.6. The position of plasma in the $\beta_{\parallel,s} - A_s$ space is changed. Both components are shifted to the region of lower beta with respect to the histogram from Figure 4.7.

Higher ion production rate: $Q_{ion} = 20 \cdot 10^{27}$ s^{-1}; $n_{atm} = 0.5 \cdot 10^{8}$ cm^{-3}

The correlation coefficient (4.2) between fluctuations of magnetic field and plasma density for the simulation *rm1-q20-sd05* with $Q_{ion} = 2 \cdot 10^{28}$ s^{-1} and $n_{atm} = 0.5 \cdot 10^{8}$ cm^{-3} is showed in the Figure 4.10. There are regions of

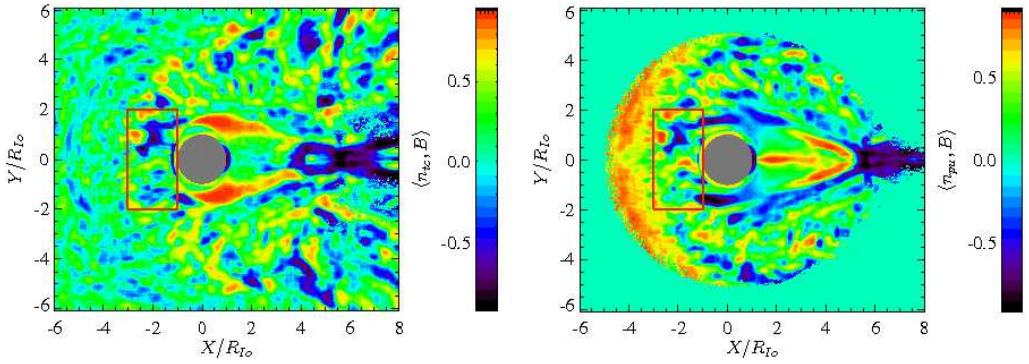

Figure 4.8: Correlation coefficient between fluctuations of magnetic field and density of torus plasma (left) or pick-up plasma from the simulation *rm1-q5-sd10*. In comparison with the Figure 4.6 which shows the correlation coefficients for simulation *rm1-q5-sd05* with lower surface neutral density, the region of strong anticorrelation vanishes because the fluctuations are reduced by high rate of charge exchanges.

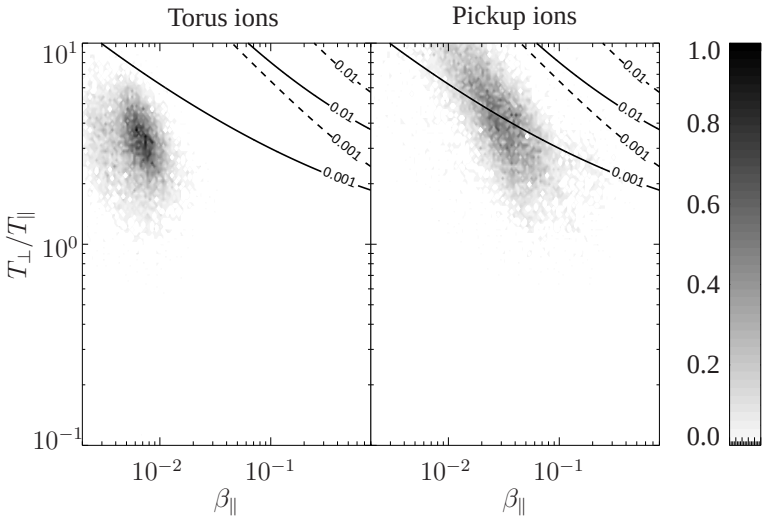

Figure 4.9: Histogram of the parallel beta versus temperature anisotropy from simulation *rm1-q5-sd05* for the cells from red box in Figure 4.8. In this simulation with high charge exchange rate both torus plasma and pick-up plasma have lower parallel beta with respect to the simulation *rm1-q5-sd05* with low charge exchange rate (see Figure 4.7).

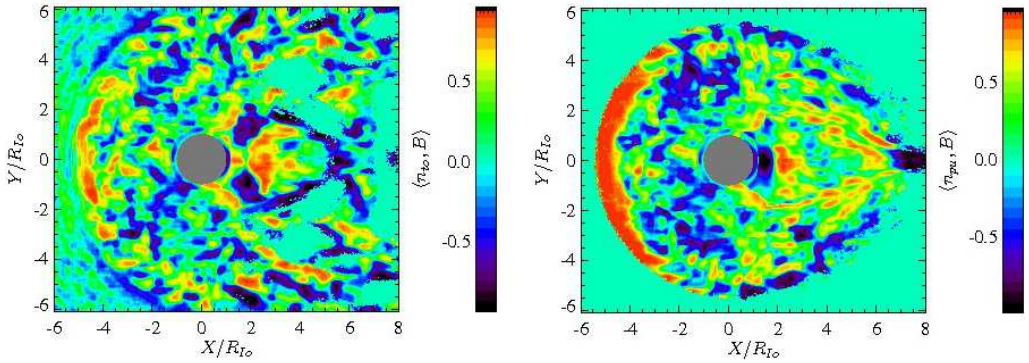

Figure 4.10: Correlation coefficient between fluctuations of magnetic field and density of torus plasma (left) or pick-up plasma (right) from the simulation *rm1-q20-sd05*. The anticorrelation of these fluctuations can be seen upstream of Io also in this simulation.

significant anticorrelation upstream of Io as in the case of lower ionization rate in the simulation *rm1-q5-sd05*. This simulation has the fluctuations spread over a larger area around Io. This effect is probably connected directly to the higher density of the pick-up plasma. In this case the parallel beta of pick-up plasma reaches the values up to $\beta_{\parallel,pu} \approx 10$ due to very high pick-up plasma densities.

Both parameters higher: $Q_{ion} = 20 \cdot 10^{27}$ s^{-1}; $n_{atm} = 10 \cdot 10^{8}$ cm^{-3}

We display the correlation coefficient (4.2) between the fluctuations of magnetic field and plasma density from the simulation *rm1-q20-sd10* with $Q_{ion} = 2 \cdot 10^{28}$ s^{-1} and $n_{atm} = 10 \cdot 10^{8}$ cm^{-3} in the Figure 4.11. The fluctuations are lower than in the simulation *rm1-q20-sd05* with same ionization rate Q_{ion} and lower surface neutral density n_{atm}. However, there can be seen region of strong anticorrelation upstream of Io. It is a difference from simulations with moderate ion production rate *rm1-q5-sd05* and *rm1-q5-sd10*. In these simulations the fluctuations were present in the case of low surface neutral density and almost vanished in the case of high surface neutral density. In this case of high ionization rate and high surface neutral density, the fluctuations are lower than in the simulation *rm1-q20-sd05* with the same ion production rate and lower surface neutral density but still exist.

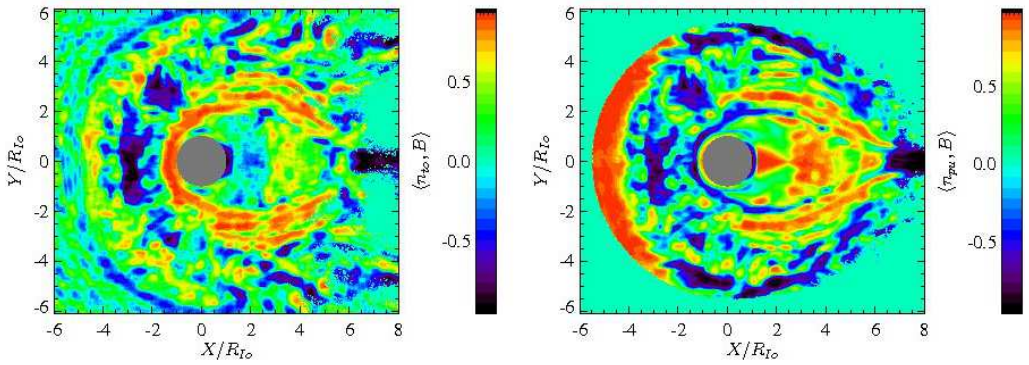

Figure 4.11: Correlation coefficient between fluctuations of magnetic field and density of torus plasma (left) or pick-up plasma (right) from the simulation *rm1-q20-sd10*. Due to the higher ion production rate than in the simulation *rm1-q5-sd10* the fluctuations are strong even though the charge exchange rate is high and significant anticorrelation between the fluctuations can be observed upstream of Io.

Lower ion production rate

Both simulations with low ion production rate $Q_{ion} = 0.5 \cdot 10^{27}$ s^{-1}, i.e., simulations *rm1-q05-sd05* and *rm1-q05-sd10*, exhibit very low level of fluctuations. The density of pick-up plasma at time $T = 500/\omega_{c,0}$ is about $n_{pu}/n_{to} \lesssim 3$ because there is very low addition of new particles in time. The density of pick-up plasma is insufficient for generation of instabilities.

No charge exchange

We performed a simulation with ion production rate $Q_{ion} = 5 \cdot 10^{27}$ s^{-1} without using a procedure for charge exchange between ions and neutrals. The resulting distribution of plasma density is similar to that of the basic simulation *rm1-q5-sd05* indicating that the charge exchange probability is weak in the case of basic simulation *rm1-q5-sd05*. This simulation and the basic simulation differ in the region close to Io which is mostly affected by the charge exchanges, the neutral density for the computation of charge exchanges is given as (4.1) with atmosphere scale height $H_{atm} = 0.5R_{Io}$. There is very low density of the torus plasma close to Io. It follows that in the simulation with no charge exchange the torus ions close to Io vanish as they either hit Io or flow away (we have showed that the plasma can flow in the opposite direction to the flow on the upstream side of Io in Figure 4.2) and the torus plasma from further regions is then unable to penetrate through the dense

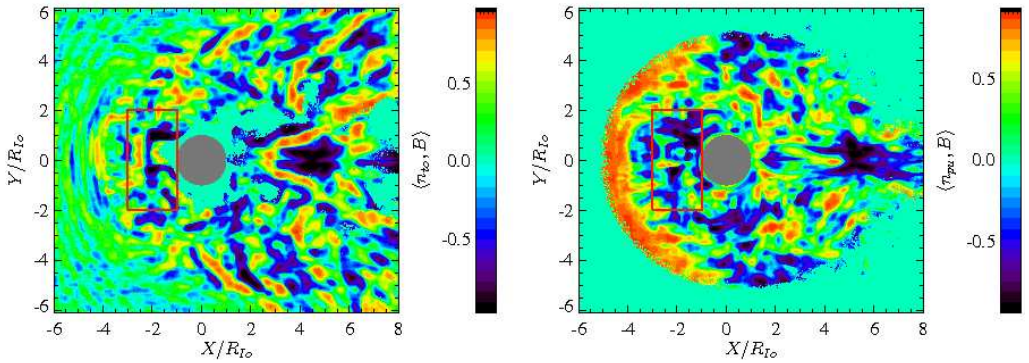

Figure 4.12: Correlation coefficient between the fluctuations of magnetic field and density of torus plasma (left) or pick-up plasma (right) from the simulation *rm1-q5-nocx*.

ionosphere near Io. The charge exchange process changes the ionic current density and thus modifies the electric field (3.2).

We show the correlation coefficient between fluctuations of magnetic field and density from the simulation *rm1-q5-nocx* with no charge exchange in Figure 4.12. The histogram of parallel beta versus temperature anisotropy is showed in Figure 4.13. The histogram is similar to that from the simulation *rm1-q5-sd05* with low surface density in Figure 4.7. In this case, the isocontour of growth rate $\gamma = 0.01\omega_c$ of the ion cyclotron instability fits better on the histogram.

Small atmosphere scale height

We have performed simulations with profile of newborn ions from electron impact ionization and photoionization as well as the profile for charge exchange of ions and neutrals given as (4.1) with $W_{int} = W_{ext} = 0.5$ and $H_{atm} = 0.1R_{Io}$. Real value of atmosphere scale height is about $H_{atm} = 0.06R_{Io}$. This profile is steeper than the profile $q(r) \propto r^{-1}$. The density of pick-up plasma has very high values at $r < 1.1R_{Io}$ but at larger distances from Io is lower in comparison to the simulation with profile $q(r) \propto r^{-1}$.

We show the correlation coefficient (4.2) between fluctuations of pick-up plasma density and magnetic field for the simulation *lip-q20-sd05* in Figure 4.14. The character of fluctuations in the simulation *lip-q20-sd10* is similar because the neutral density falls off rapidly with increasing distance so the probability of charge exchange further from Io is very small for both values of surface neutral density.

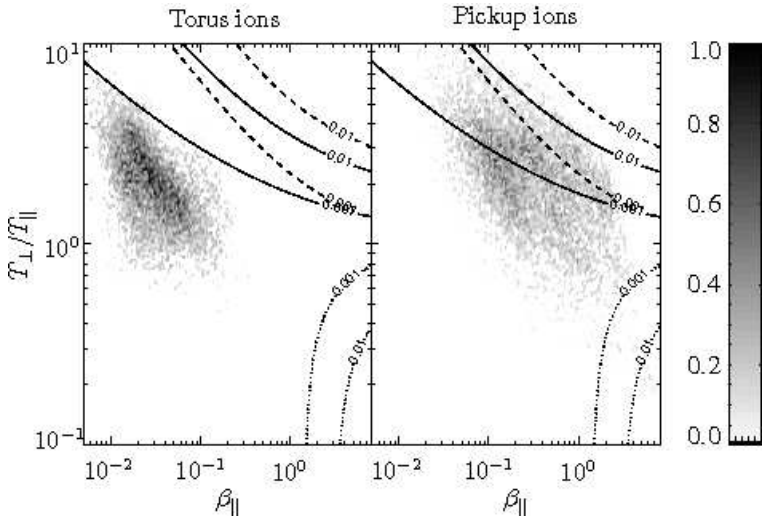

Figure 4.13: Histogram of the parallel beta versus temperature anisotropy for the cells from red box in Figure 4.12. In contrary to the simulation with low surface neutral density (i.e., low charge exchange rate) from the Figure 4.7 the pick-up plasma is constrained rather with the isocontour of the growth rate $\gamma = 0.01\omega_c$ of the ion cyclotron instability.

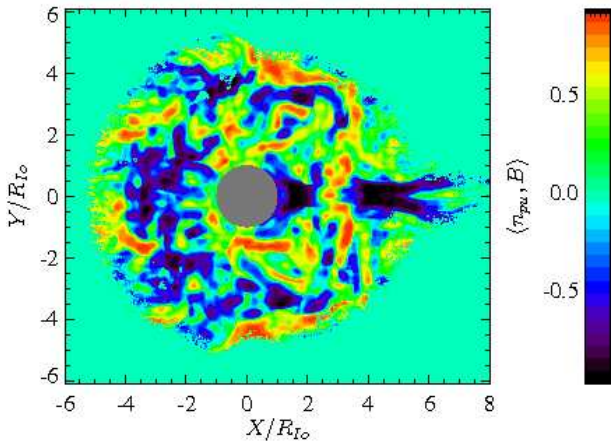

Figure 4.14: Correlation coefficient between fluctuations of pick-up plasma density and magnetic field from the simulation *lip-q20-sd05* with ion production rate profile given as (4.1). There is significant anticorrelation between fluctuations upstream of Io.

Discussion and conclusions

We have studied the interaction between Jupiter moon Io and its plasma torus. The work contains an introduction to the theory of instabilities driven by temperature anisotropy of ions and a review of the Io's plasma environment properties.

We used hybrid two-dimensional simulation code with kinetic ions and fluid electrons to study the interaction. We have performed a set of simulations with different properties of Io's neutral atmosphere and ionosphere. We used variable ion production rate due to the photoionization and electron impact ionization and variable density of neutral atmosphere to change the rate of charge exchanges between ions and neutrals. We have studied effects of these parameters on the plasma at Io and properties of fluctuations close to Io.

We have showed a global features of the interaction between the plasma torus and Io including the compression of the magnetic field upstream of Io and expansion downstream of Io, deceleration and divertion of the torus plasma flow upstream of Io and pulling of the pick-up plasma by the torus flow.

We have focused on evolution of temperature anisotropy of plasma and properties of fluctuations at Io. The temperature anisotropy of both torus plasma and pick-up plasma has moderate values about $T_\perp/T_\parallel \lesssim 5$ in the regions of highest fluctuations. The torus plasma has very low parallel beta $\beta_{\parallel,to} \lesssim 0.06$ and thus lies below the thresholds of ion cyclotron and mirror instability. The pick-up plasma has larger parallel beta than the torus plasma because of larger density so that the pick-up plasma reaches to the region unstable to the ion cyclotron and mirror modes.

There are very low fluctuations in simulations with low ion production rate $Q_{ion} = 5 \cdot 10^{26}$. We observe fluctuations of magnetic field and plasma density in simulations with moderate and high ion production rate $Q_{ion} = 5 \cdot 10^{27}$ s^{-1} and $Q_{ion} = 2 \cdot 10^{27}$ s^{-1}. These fluctuations are present mainly on the upstream side and their amplitude decreases to Io's poles. The amplitude of fluctuations is very low on the downstream side. Fluctuations are spread

over larger area in simulations with high ion production rate $Q_{ion} = 2 \cdot 10^{28}$ s^{-1} than in simulations with moderate ion production rate $Q_{ion} = 5 \cdot 10^{27}$ s^{-1}. Considering the fact that fluctuations are not present in simulations with low ion production rate $Q_{ion} = 5 \cdot 10^{26}$, it follows that the growth of fluctuations depends on the density of newborn pick-up plasma. This fact may indicate that fluctuations result from the activity of temperature anisotropy driven instabilities.

In order to study properties of fluctuations, we have computed the Pearson correlation coefficient between fluctuations of plasma density and magnitude of magnetic field. In some simulations we observe regions of significant anticorrelation between these fluctuations. The region of anticorrelation is most evident in the simulation with ion production rate profile given as $q(r) \propto r^{-1}$ and moderate ion production rate $Q_{ion} = 5 \cdot 10^{27}$ s^{-1} and low surface neutral density $n_{atm} = 0.5 \cdot 10^8$ cm^{-3}. In the simulation with the same ion production rate and higher surface neutral density $n_{atm} = 10 \cdot 10^8$ cm^{-3}, fluctuations are reduced and the region of anticorrelation almost vanishes. We observe anticorrelation between fluctuations of magnetic field and plasma density in both simulations with high ion production rate $Q_{ion} = 2 \cdot 10^{28}$ s^{-1}. The fluctuations are lower in the case of higher surface neutral density. We have performed simulations with ion production rate profile with lower atmosphere scale height $H_{atm} = 0.1 R_{Io}$. We have observed significant anticorrelation in simulations with high ion production rate $Q_{ion} = 2 \cdot 10^{28}$ s^{-1}. In these simulations the character of fluctuations is not influenced by the value of surface neutral density. Fluctuations grow further from Io where the charge exchange rate is negligible for both values of surface neutral density. The anticorrelation between fluctuations may indicate the growth of mirror instability.

In conclusions, we observe the wave activity mainly upstream of Io. Observations of *Galileo* indicate that temperature anisotropy driven instabilities are active rather on the downstream side of Io. However, it is hard to compare the results of these two-dimensional simulations with the measurements of *Galileo*. Only the I31 flyby was parallel to the flow but its trajectory was shifted from the axis of torus plasma to the anti-Jovian side so it did not lie in the plane of our simulations. The trajectory of the I0 flyby intersects the plane of our simulations at distance $1.5 R_{Io}$ in the wake. *Galileo* observed very low wave activity at this location. The trajectory of I31 flyby intersects the plane of our simulations at $1.5 R_{Io}$ upstream of Io and *Galileo* detected a short burst of ion cyclotron waves at this location.

This work will continue by implementing a three-dimensional version of the code. Great advantage of the three-dimensional code is that it provides possibility of comparing the simulation data with real data measured in situ

by the satellite *Galileo* thus allowing to tune working parameters to real values. On the other hand, the three-dimensional code enables to model relatively smaller plasma and the situation will probably require implementation of open boundary conditions to maintain the high resolution required to study the plasma kinetic effects.

We plan to use more precise composition of the plasma torus using more plasma species. The composition of Io's atmosphere and ionosphere is radially variable as different neutral and plasma species have different radial decrease depending on the various chemistry of particular neutrals and ions with other ions, electrons and photons. The implementation of charge exchange chemistry between ions and different neutral species as well as between various ionic species will be probably required to fit the wave observations of *Galileo*.

Bibliography

Anderson, B. J. and Fuselier, S. A. (1993). Magnetic pulsations from 0.1 to 4.0 hz and associated plasma properties in the Earth's subsolar magnetosheath and plasma depletion layer. *J. Geophys. Res.*, 98(A2):1461–1479.

Bagenal, F. (1994). Empirical model of the Io plasma torus: Voyager measurements. *J. Geophys. Res.*, 99(A6):11043–11062.

Bagenal, F. (1997). The ionization source near Io from Galileo wake data. *Geophys. Res. Lett.*, 24(17):2111–2114.

Bale, S. D., Kasper, J. C., Howes, G. G., Quataert, E., Salem, C., and Sundkvist, D. (2009). Magnetic fluctuation power near proton temperature anisotropy instability thresholds in the solar wind. *Phys. Rev. Lett.*, 103:211101.

Baumjohann, W. and Treumann, R. A., editors (1996). *Basic Space Plasma Physics*. Imperial College Press, London, UK.

Blanco-Cano, X., Russell, C. T., Strangeway, R. J., Kivelson, M. G., and Khurana, K. K. (2001). Galileo observations of ion cyclotron waves in the Io torus. *Adv. Space Res.*, 28(10):1469–1474.

Brown, R. A. (1974). Optical line emission from Io. *Exploration of the Planetary system*, 65:527–531.

Combi, M. R., Kabin, K., Gombosi, T. I., DeZeeuw, D. L., and Powell, K. G. (1998). Io's plasma environment during the Galileo flyby: Global three-dimensional MHD modeling with adaptive mesh refinement. *J. Geophys. Res.*, 103(A5):9071–9081.

Crary, F. J., Bagenal, F., Frank, L. A., and Paterson, W. R. (1998). Galileo plasma spectrometer measurements of composition and temperature in the Io plasma torus. *J. Geophys. Res.*, 103(A12):29359–29370.

Delamere, P. A. and Bagenal, F. (2003). Modeling variability of plasma conditions in the Io torus. *J. Geophys. Res.*, 108(A7):1276.

Drell, S. D., Foyle, H. M., and Ruderman, M. A. (1965). Drag and propulsion of large satellites in the ionosphere: An Alfvén propulsion engine in Space. *J. Geophys. Res.*, 70(13):3131–3145.

Frank, L. A. and Paterson, W. R. (2001a). Passage through Io's ionospheric plasmas by the Galileo spacecraft. *J. Geophys. Res.*, 106(A11):26209–26224.

Frank, L. A. and Paterson, W. R. (2001b). Survey of thermal ions in the Io plasma torus with the Galileo spacecraft. *J. Geophys. Res.*, 106(A4):6131–6149.

Gary, S. P., editor (1993). *Theory of Space Plasma Microinstabilities*. Cambridge University Press, New York, NY.

Gary, S. P., Fuselier, S. A., and Anderson, B. J. (1993). Ion anisotropy instabilities in the magnetosheath. *J. Geophys. Res.*, 98(A2):1481–1488.

Gary, S. P. and Lee, M. A. (1994). The ion cyclotron anisotropy instability and the inverse correlation between proton anisotropy and proton beta. *J. Geophys. Res.*, 99(A6):11297–11301.

Gary, S. P., Li, H., O'Rourke, S., and Winske, D. (1998). Proton resonant firehose instability: Temperature anisotropy and fluctuating field constraints. *J. Geophys. Res.*, 103(A7):14567–14574.

Gary, S. P., Skoug, R. M., Steinberg, J. T., and Smith, C. W. (2001). Proton temperature anisotropy constraint in the solar wind: ACE observation. *Geophys. Res. Lett.*, 28(14):2759–2762.

Génot, V., Budnik, E., Hellinger, P., Passot, T., Belmont, G., Trávníček, P. M., Sulem, P.-L., Lucek, E., and Dandouras, I. (2009). Mirror structures above and below the linear instability threshold: Cluster observations, fluid model and hybrid simulations. *Ann. Geophys.*, 27(2):601–615.

Goldstein, M. L., Wong, H. K., Vinas, A. F., and Smith, C. W. (1985). Large-amplitude MHD waves upstream of the Jovian bow shock: Reinterpretation. *J. Geophys. Res.*, 90(A1):302–310.

Gratiy, S. L., Walker, A. C., Levin, D. A., Goldstein, D. B., Varghese, P. L., Trafton, L. M., and Moore, C. H. (2010). Multi-wavelength simulations of

atmospheric radiation from Io with a 3-D spherical-shell backward Monte Carlo radiative transfer model. *Icarus*, 207:394–408.

Gurnett, D. A., Kurth, W. S., Roux, A., Bolton, S. J., and Kennel, C. F. (1996). Galileo plasma wave observations in the Io plasma torus and near Io. *Science*, 274(5286):391–392.

Hasegawa, A. (1969). Drift mirror instability in the magnetosphere. *Phys. Fluids*, 12(12):2642–2650.

Hellinger, P. (2007). Comment on the linear mirror instability near the threshold. *Phys. Plasmas*, 14(8):082105.

Hellinger, P. (2008). Comment on the drift mirror instability. *Phys. Plasmas*, 15(5):054502.

Hellinger, P. and Matsumoto, H. (2000). New kinetic instability: Oblique Alfvén fire hose. *J. Geophys. Res.*, 105(A5):10519–10526.

Hellinger, P., Trávníček, P., Kasper, J. C., and Lazarus, A. J. (2006). Solar wind proton temperature anisotropy: Linear theory and WIND/SWE observations. *Geophys. Res. Lett.*, 33(9):L09101.

Hill, P., Paschmann, G., Treumann, R. A., Baumjohann, W., Sckopke, N., and Lűhr, H. (1995). Plasma and magnetic field behavior across the magnetosheath near local noon. *J. Geophys. Res.*, 100(A6):9575–9583.

Hinson, D. P., Kliore, A. J., Flasar, F. M., Twicken, J. D., Schneider, P. J., and Herrera, R. G. (1998). Galileo radio occultation measurements of Io's ionosphere and plasma wake. *J. Geophys. Res.*, 103(A12):29343–29357.

Huddleston, D. E., Strangeway, R. J., Blanco-Cano, X., Russell, C. T., Kivelson, M. G., and Khurana, K. K. (1999). Mirror-mode structures at the Galileo-Io flyby: Instability criterion and dispersion analysis. *J. Geophys. Res.*, 104(A8):17479–17489.

Huddleston, D. E., Strangeway, R. J., Warnecke, J., Russell, C. T., and Kivelson, M. G. (1997). Ion cyclotron waves in the Io torus during the Galileo encounter: Warm plasma dispersion analysis. *Geophys. Res. Lett.*, 24(17):2143–2146.

Huddleston, D. E., Strangeway, R. J., Warnecke, J., Russell, C. T., and Kivelson, M. G. (1998). Ion cyclotron waves in the Io torus: Wave dispersion, free energy analysis, and SO_2^+ source rate estimates. *J. Geophys. Res.*, 103(E9):19887–19899.

Jessup, K. L., Spencer, J. R., Ballester, G. E., Howell, R. R., Roesler, F., Vigel, M., and Yelle, R. (2004). The atmospheric signature of Io's Prometheus plume and anti-jovian hemisphere: Evidence for a sublimation atmosphere. *Icarus*, 169:197–215.

Joy, S. P., Kivelson, M. G., Walker, R. J., Khurana, K. K., Russell, C. T., and Paterson, W. R. (2006). Mirror mode structures in the Jovian magnetosheath. *J. Geophys. Res.*, 111:A12212.

Kabin, K., Combi, M. R., Gombosi, T. I., DeZeeuw, D. L., Hansen, K. C., and Powell, K. G. (2001). Io's magnetospheric interaction: an MHD model with day-night asymmetry. *Planet. Space Sci.*, 49:337–344.

Kasper, J. C., Lazarus, A. J., and Gary, S. P. (2002). Wind/swe observations of firehose constraint on solar wind proton temperature anisotropy. *Geophys. Res. Lett.*, 29(17):1839.

Kivelson, M. G., Bagenal, F., Kurth, W. S., Neubauer, F. M., Paranicas, C., and Saur, J. (2004). Magnetospheric Interactions with Satellites. In Bagenal, F., Dowling, T., and McKinnon, W., editors, *Jupiter: the Planet, Sattelites and Magnetosphere*, pages 513–536. Cambridge University Press, New York, NY.

Linker, J. A., Khurana, K. K., Kivelson, M. G., and Walker, R. J. (1998). MHD simulations of Io's interaction with the plasma torus. *J. Geophys. Res.*, 103(E9):19867–19877.

Linker, J. A., Kivelson, M. G., Moreno, M. A., and Walker, R. J. (1985). Explanation of the inward displacement of Io's hot plasma torus and consequences for sputtering sources. *Nature*, 315:373–378.

Linker, J. A., Kivelson, M. G., and Walker, R. J. (1989). The effect of mass loading on the temperature of flowing plasma. *Geophys. Res. Lett.*, 16(7):763–766.

Linker, J. A., Kivelson, M. G., and Walker, R. J. (1991). A three-dimensional MHD simulation of plasma flow past Io. *J. Geophys. Res.*, 96(A12):21037–21053.

Lipatov, A. S. and Combi, M. R. (2006). Effects of kinetic processes in shaping Io's global plasma environment: A 3D hybrid model. *Icarus*, 180:412–427.

Lipatov, A. S., Zank, G. P., and Pauls, H. L. (1998). The interaction of neutral interstellar H with the heliosphere: A 2.5-D particle-mesh boltzmann simulation. *J. Geophys. Res.*, 103(A9):20631–20642.

Matthews, A. P. (1994). Current advance method and cyclic leapfrog for 2d multispecies hybrid plasma simulations. *J. Comp. Phys.*, 112:102–116.

McKean, M. E., Winske, D., and Gary, S. P. (1992). Kinetic properties of mirror waves in magnetosheath plasmas. *Geophys. Res. Lett.*, 19(13):1331–1334.

Morabito, L. A., Synnott, S. P., Kupferman, P. N., and Collins, S. A. (1979). Discovery of currently active extraterrestrial volcanism. *Science*, 204:972.

Neubauer, F. M. (1980). Nonlinear standing Alfvén wave current system at Io: Theory. *J. Geophys. Res.*, 85(A3):1171–1178.

Peale, S. J., Cassen, P., and Reynolds, R. T. (1979). Melting of Io by tidal dissipation. *Science*, 203:892–894.

Pearl, J., Hanel, R., Kunde, V., Maguire, W., Fox, K., Gupta, S., Ponnamperuma, C., and Raulin, F. (1979). Identification of gaseous SO_2 and new upper limits for other gases on Io. *Nature*, 280:755–758.

Price, C. P., Swift, D. W., and Lee, L.-C. (1986). Numerical simulation of nonoscillatory mirror waves at the Earth's magnetosheath. *J. Geophys. Res.*, 91(A1):101–112.

Ripken, H. W. and Fahr, H. J. (1983). Modification of the local interstellar gas properties in the heliospheric interface. *Astron. Astrophys.*, 122:181–192.

Russell, C. T., Blanco-Cano, X., and Kivelson, M. G. (2003a). Ion cyclotron waves in Io's wake region. *Planet. Space Sci.*, 51:233–238.

Russell, C. T., Blanco-Cano, X., Wang, Y. L., and Kivelson, M. G. (2003b). Ion cyclotron waves at Io: Implications for the temporal variation of Io's atmosphere. *Planet. Space Sci.*, 51:937–944.

Russell, C. T., Huddleston, D. E., Strangeway, R. J., Blanco-Cano, X., Kivelson, M. G., Khurana, K. K., Frank, L. A., Paterson, W., Gurnett, D. A., and Kurth, W. S. (1999a). Mirror-mode structures at the Galileo-Io flyby: Observations. *J. Geophys. Res.*, 104(A8):17471–17477.

Russell, C. T., Kivelson, M. G., Khurana, K. K., and Huddleston, D. E. (1999b). Magnetic fluctuations close to Io: Ion cyclotron and mirror mode wave properties. *Planet. Space Sci.*, 47:143–150.

Russell, C. T., Leisner, J. S., Arridge, C. S., Dougherty, M. K., and Blanco-Cano, X. (2006). Nature of magnetic fluctuations in Saturn's middle magnetosphere. *J. Geophys. Res.*, 111:A12205.

Saur, J., Neubauer, F. M., Connerney, J. E. P., Zarka, P., and Kivelson, M. G. (2004). Plasma Interaction of Io with its Plasma Torus. In Bagenal, F., Dowling, T., and McKinnon, W., editors, *Jupiter: the Planet, Satellites and Magnetosphere*, pages 537–560. Cambridge University Press, New York, NY.

Saur, J., Neubauer, F. M., Strobel, D. F., and Summers, M. E. (1999). Three dimensional plasma simulation of Io's interaction with the Io plasma torus: Asymmetric plasma flow. *J. Geophys. Res.*, 104(A11):25105–25126.

Saur, J., Neubauer, F. M., Strobel, D. F., and Summers, M. E. (2002). Interpretation of Galileo's Io plasma and field observations: I0, I24, and I27 flybys and close polar passes. *J. Geophys. Res.*, 107:1422.

Saur, J. and Strobel, D. F. (2004). Relative contributions of sublimation and volcanoes to Io's atmosphere inferred from its plasma interaction during solar eclipse. *Icarus*, 171:411–420.

Saur, J., Strobel, D. F., Neubauer, F. M., and Summers, M. E. (2003). The ion mass loading rate at Io. *Icarus*, 163:456–468.

Sittler, E. C. and Strobel, D. F. (1987). Io plasma torus electrons: Voyager 1. *J. Geophys. Res.*, 92(A6):5741–5762.

Smyth, W. H. and Wong, M. C. (2004). Impact of electron chemistry on the structure and composition of Io's atmosphere. *Icarus*, 171:171–182.

Southwood, D. J. and Kivelson, M. G. (1993). Mirror instability: 1. Physical mechanism of linear instability. *J. Geophys. Res.*, 98(A6):9181–9187.

Southwood, D. J., Kivelson, M. G., Walker, R. J., and Slavin, J. A. (1980). Io and its plasma environment. *J. Geophys. Res.*, 85(A11):5959–5968.

Spencer, J. R., Jessup, K. L., McGrath, M. A., Ballester, G. E., and Yelle, R. (2000). Discovery of gaseous S_2 in Io's Pele plume. *Science*, 288(5469):1208–1210.

Spencer, J. R., Lellouch, E., Richter, M. J., López-Valverde, M. A., Jessup, K. L., Greathouse, T. K., and Flaud, J. M. (2005). Mid-infrared detection of large longitudinal asymmetries in Io's SO_2 atmosphere. *Icarus*, 176:283–304.

Steffl, A. J., Bagenal, F., and Stewart, A. I. F. (2004). Cassini UVIS observations of the Io plasma torus. II. Radial variations. *Icarus*, 172:91–103.

Strom, R. G., Terrile, R. J., Masursky, H., and Hansen, C. (1979). Volcanic eruption plumes on Io. *Nature*, 280:733–736.

Trávníček, P. M., Hellinger, P., and Schriver, D. (2007). Structure of Mercury's magnetosphere for different pressure of the solar wind: Three dimensional hybrid simulations. *Geophys. Res. Lett.*, 34:L05104.

Trávníček, P. M., Hellinger, P., Schriver, D., and Bale, S. D. (2005). Structure of the lunar wake: Two-dimensional global hybrid simulations. *Geophys. Res. Lett.*, 32:L06102.

Treumann, R. A. and Baumjohann, W., editors (1997). *Advanced Space Plasma Physics*. Imperial College Press, London, UK.

Walker, A. C., Gratiy, S. L., Goldstein, D. B., Moore, C. H., Varghese, P. L., Trafton, L. M., Levin, D. A., and Stewart, B. (2010). A comprehensive numerical simulation of Io's sublimation-driven atmosphere. *Icarus*, 207:409–432.

Warnecke, J., Kivelson, M. G., Khurana, K. K., Huddleston, D. E., and Russell, C. T. (1997). Ion cyclotron waves observed at Galileo's Io encounter: Implications for neutral cloud distribution and plasma composition. *Geophys. Res. Lett.*, 24(17):2139–2142.

Williams, D. J., Thorne, R. M., and Mauk, B. (1999). Energetic electron beams and trapped electrons at Io. *J. Geophys. Res.*, 104(A7):14739–14753.

Winterhalter, D., Neugebauer, M., Goldstein, B. E., Smith, E. J., Bame, S. J., and Balogh, A. (1994). Ulysses field and plasma observations of magnetic holes in the solar wind and their relation to mirror-mode structures. *J. Geophys. Res.*, 99(A12):23371–23381.